Immunity
Article

MicroRNAs Prevent the Generation of Autoreactive Antibodies

Laura Belver,[1] Virginia G. de Yébenes,[1] and Almudena R. Ramiro[1,*]
[1]DNA Hypermutation and Cancer Group. Spanish National Cancer Research Center (CNIO), Madrid 28029, Spain
*Correspondence: aramiro@cnio.es
DOI 10.1016/j.immuni.2010.11.010

SUMMARY

MicroRNAs have been shown to be critical for a number of aspects of immune system regulation and function. Here, we have examined the role of microRNAs in terminal B cell differentiation by analyzing *Cd19*-Cre$^{ki/+}$ *Dicer1*$^{fl/fl}$ mice. We found that in the absence of Dicer, the transitional and marginal zone (MZ) B cell compartments were overrepresented and follicular (FO) B cell generation was impaired. microRNA analysis revealed that miR185, a microRNA overexpressed in FO cells, dampened B cell receptor (BCR) signaling through Bruton tyrosine kinase downregulation. Dicer-deficient B cells had a skewed BCR repertoire with hallmarks of autoreactivity, which correlated with high titers of autoreactive antibodies in serum and autoimmune features in females. Together, our results reveal a crucial role for microRNAs in late B cell differentiation and in the establishment of B cell tolerance.

INTRODUCTION

Primary antibody diversification is generated during B cell differentiation in the bone marrow through somatic DNA rearrangement of immunoglobulin (Ig) genes by V(D)J recombination (Bassing et al., 2002). Because of its stochastic nature, antibody diversification can give rise to B cell antigen receptors (BCRs) that recognize the body's self components and potentially lead to autoimmunity. This pathological outcome is usually prevented by tolerance mechanisms that are governed by signals delivered by the BCR (Gu et al., 1991; Hartley et al., 1991; Meffre et al., 2000; Meffre and Wardemann, 2008; Shlomchik, 2008; Wardemann and Nussenzweig, 2007). Two main checkpoints ensure B cell tolerance: one is established in the bone marrow in early immature B cells that have completed V(D)J recombination of heavy and light Ig genes (Goodnow et al., 1988; Nemazee and Bürki, 1989; Wardemann et al., 2003), and the second takes place in peripheral B cells in transit to their final maturation (Wardemann et al., 2003). At this late maturation stage, transitional B cells can give rise to two functionally distinct peripheral populations: follicular (FO) or marginal zone (MZ) B cells (Allman and Pillai, 2008; Carsetti et al., 2004). FO versus MZ fate decision is functionally coupled to BCR signaling (Carsetti et al., 2004; Pillai and Cariappa, 2009), and it has been suggested that B cells bearing BCRs with autoreactive specificities are preferentially driven into a MZ fate (Li et al., 2002; Martin and Kearney, 2000). However, the molecular mechanisms that regulate this transition and its link to B cell tolerance establishment remain poorly understood.

MicroRNAs are small RNA (21–22 nucleotides long) posttranscriptional regulators of gene expression, which have been unveiled to be critical for numerous aspects of the regulation and maintenance of the mammalian immune system (Martinez and Busslinger, 2007; Xiao and Rajewsky, 2009). Mature microRNAs are generated through the sequential cleavage of longer RNA precursors by Drosha and Dicer (gene name *Dicer1*) RNA endonucleases (Kim et al., 2009). Early Dicer ablation in the B cell lineage results in an almost complete block of B cell differentiation at the pro-B cell stage; such a block is due to an aberrant regulation of apoptosis in the bone marrow (Koralov et al., 2008). These results highlight the essential role of microRNAs in B cell generation in the bone marrow; however, the severity of the phenotype precluded the analysis of terminal B cell differentiation and selection.

Here, we have addressed the role of microRNAs at late B cell differentiation stages in *Cd19*-Cre$^{ki/+}$*Dicer1*$^{fl/fl}$ mice, which allowed B cell-specific Dicer deletion. Mature B cells were generated in *Cd19*-Cre$^{ki/+}$ *Dicer1*$^{fl/fl}$ mice, in which transitional and MZ B cells were overrepresented and the generation of FO B cells was impaired. MicroRNA analysis revealed that miR185, a microRNA differentially expressed in FO versus MZ B cells, promoted downregulation of the BCR signaling effector Bruton tyrosine kinase (Btk) in activated B cells. Importantly, Dicer-deficient B cells produced high titers of autoreactive antibodies, which correlated with the presence of autoimmune features in aged female animals. Therefore, our results provide evidence for a role of microRNAs in terminal B cell differentiation and in the establishment of B cell tolerance.

RESULTS

Mature B Cells Are Generated in *Cd19*-Cre$^{ki/+}$ *Dicer1*$^{fl/fl}$ Mice

To address the function of microRNAs at late stages of B cell development, we generated B cell-specific Dicer-deficient mice by breeding *Cd19*-Cre$^{ki/+}$ (Rickert et al., 1997) to *Dicer1*$^{fl/fl}$ mice (Harfe et al., 2005). *Cd19*-Cre-mediated deletion takes place gradually during bone marrow differentiation (Hobeika et al., 2006; Schmidt-Supprian and Rajewsky, 2007) in contrast to Dicer ablation by *Cd79a*-Cre (also known as *mb1*-Cre)

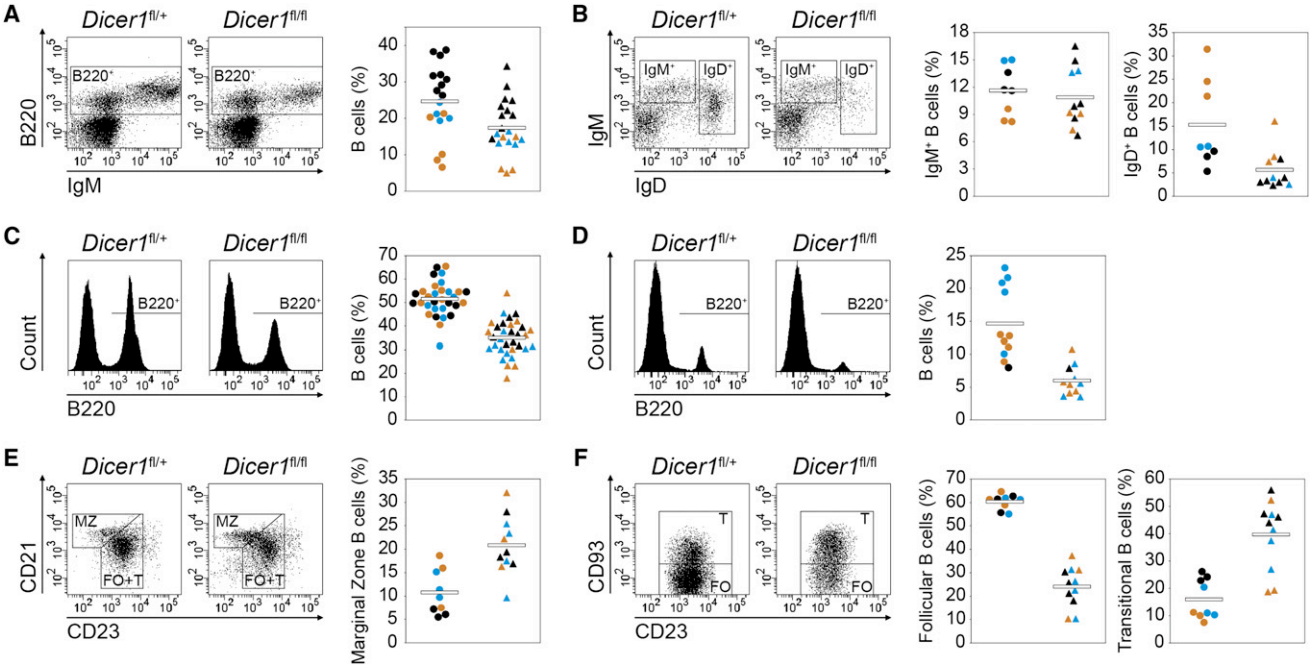

Figure 1. Total Peripheral B Cells Are Reduced and MZ and T Subsets Are Overrepresented in the Absence of Dicer

Phenotypic analysis of bone marrow (A and B), spleen (C, E, and F) and lymph nodes (D) from *Cd19*-Cre$^{ki/+}$ *Dicer1*$^{fl/+}$ and *Cd19*-Cre$^{ki/+}$ *Dicer1*$^{fl/fl}$ mice. Cell suspensions were stained with the indicated antibodies and analyzed by flow cytometry. Representative FACS analyses are shown on the left for total cells (A, C, and D), B220$^+$-gated cells (B and E), or B220$^+$CD23^{bright}-gated cells (F). Graphs on the right show the frequency of the indicated subsets in individual mice analyzed as follows: (A) B220$^+$ bone marrow B cells (n = 18–21, p = 0.01); (B) IgM$^+$IgD$^-$ immature B (n = 8–11, p = 0.62) and IgD$^+$ recirculating B cells (n = 8–11, p < 0.01); (C) B220$^+$ spleen B cells (n = 31-33, p < 0.01); (D) B220$^+$ lymph node cells (n = 11, p < 0.01); (E) CD21^{bright}CD23$^+$ marginal zone (MZ) (n = 9–11, p < 0.01); and (F) CD21$^+$CD23^{bright}CD93$^-$ follicular (FO) (n = 9–11, p < 0.01), and CD21$^+$CD23^{bright}CD93$^+$ transitional (T) cells (n = 9–11, p < 0.01) within total spleen B cells. Circles represent *Cd19*-Cre$^{ki/+}$ *Dicer1*$^{fl/+}$ mice and triangles represent *Cd19*-Cre$^{ki/+}$ *Dicer1*$^{fl/fl}$ mice. Color code represents mouse age (black, < 10 weeks old; blue, 10 to 20 weeks old; and orange, > 20 weeks old). Mean values are shown as horizontal bars. See also Figure S1 and Table S1.

(Koralov et al., 2008), which promotes deletion of close to 100% of bone marrow B lineage cells (Hobeika et al., 2006) from the pro-B cell stage (Koralov et al., 2008). Consistently, *Cd19*-Cre$^{ki/+}$ *Dicer1*$^{fl/fl}$ mice showed a substantial depletion (86% reduction) of Dicer mRNA in immature B220$^+$IgM$^+$ bone marrow cells but not at earlier differentiation stages (Figure S1A available online). Analysis of bone marrow revealed a mild reduction of total B220$^+$ cells in *Cd19*-Cre$^{ki/+}$ *Dicer1*$^{fl/fl}$ mice (Figure 1A), although percentages of pro-B, pre-B, and immature IgM$^+$ cells were normal (Figures S1B and S1C and Figure 1B). In contrast, the proportion of recirculating IgD$^+$ cells was reduced in *Cd19*-Cre$^{ki/+}$ *Dicer1*$^{fl/fl}$ mice to 35% of control values (19.7% ± 10.0% versus 7.0% ± 4.8%) (Figure 1B), suggesting that the reduced number of B220$^+$ cells in Dicer-deficient bone marrow was mostly accounted for by a defect in the generation of mature B cells, rather than in earlier stages. In agreement with these results, the percentage of peripheral B cells was decreased in spleen and lymph nodes in *Cd19*-Cre$^{ki/+}$ *Dicer1*$^{fl/fl}$ mice (spleen, 50.2% ± 7.2% versus 35.0% ± 7.5%; lymph nodes, 14.7% ± 5.6% versus 6.0% ± 2.3%, Figures 1C and 1D), with absolute spleen B cell numbers reduced to 41% of those in control animals (Figure S1D and Table S1). Non-B cell subsets, including T regulatory cells, were present in normal numbers and showed normal Dicer expression in *Cd19*-Cre$^{ki/+}$ *Dicer1*$^{fl/fl}$ mice (Figures S1D–S1I), indicating that Dicer was specifically depleted in the B cell lineage in this model. No differences were observed when *Cd19*-Cre$^{ki/+}$ *Dicer1*$^{fl/+}$ mice were compared to *Cd19*-Cre$^{ki/+}$ *Dicer1*$^{+/+}$ mice (data not shown). Therefore, Dicer depletion in *Cd19*-Cre$^{ki/+}$ *Dicer1*$^{fl/fl}$ mice is compatible with the generation of peripheral B cells, but their number is severely reduced.

Peripheral B Cell Subsets Are Shifted in *Cd19*-Cre$^{ki/+}$ *Dicer1*$^{fl/fl}$ Mice

Once in the periphery, transitional IgM$^+$ B cells progressively start expressing IgD and terminally differentiate into either MZ or FO B cells (Carsetti et al., 2004; Su et al., 2004). FO or conventional B cells (CD21$^+$CD23^{bright}CD93$^-$) populate the inner follicle and are associated to T cell-dependent immune responses. In contrast, MZ B cells (CD21^{bright}CD23$^+$) are recruited to the outer layer of spleen follicles and provide a first and rapid response against blood-borne antigens (Martin et al., 2001). In addition, a third B cell subset, called B1 cells, populates the spleen and peritoneal cavities and is believed to contribute with natural antibodies to T cell-independent responses (Allman and Pillai, 2008; Martin et al., 2001). Both MZ and B1 cells have been associated with the generation of self-reactive antibodies (Allman and Pillai, 2008; Dammers et al., 2000; Hayakawa et al., 1984; Li et al., 2002; Martin and Kearney, 2000). We found that in *Cd19*-Cre$^{ki/+}$ *Dicer1*$^{fl/fl}$ mice the percentage of spleen transitional B cells (CD21$^+$CD23^{bright}CD93$^+$) was increased (39.8% ± 12.8% versus

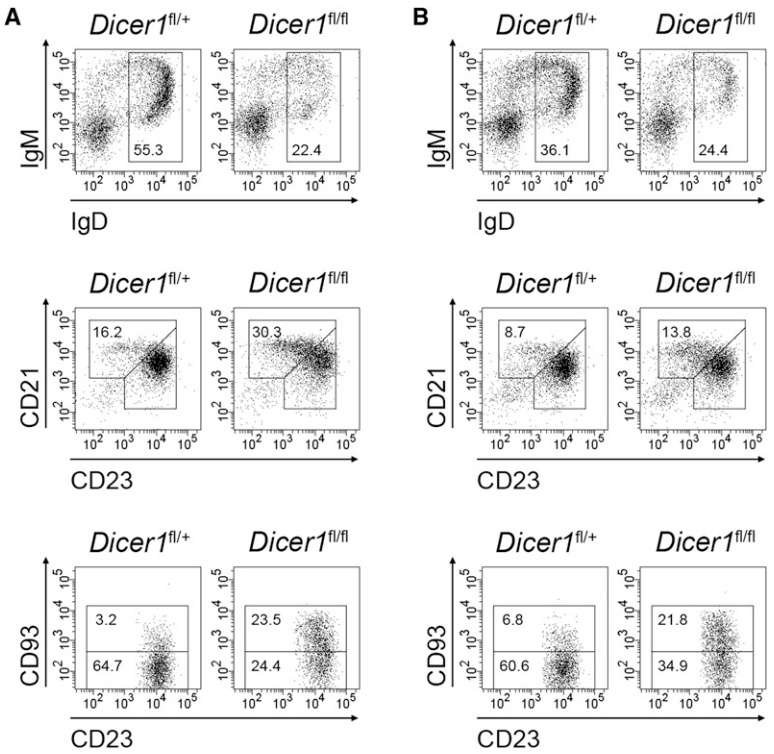

Figure 2. Dicer-Deficient Cells in Mixed Chimeras Show a Reduction in Total Peripheral B Cell Generation and an Overrepresentation of MZ and T Cell Subsets

Phenotypic analysis of bone marrow and spleen from lethally irradiated mice 12 weeks after bone marrow transfer with 100% CD45.2$^+$ *Cd19*-Cre$^{ki/+}$ *Dicer1*$^{fl/+}$ or 100% CD45.2$^+$ *Cd19*-Cre$^{ki/+}$ *Dicer1*$^{fl/fl}$ cells (A) and 1:1 mixtures of bone marrow cells from CD45.2$^+$ *Cd19*-Cre$^{ki/+}$ *Dicer1*$^{fl/+}$ or CD45.2$^+$ *Cd19*-Cre$^{ki/+}$ *Dicer1*$^{fl/fl}$ mice with bone marrow cells from CD45.1$^+$ wild-type mice (B). Representative FACS analyses for the indicated markers are shown for B220$^+$-gated CD45.2$^+$ bone marrow cells (top histograms), B220$^+$-gated CD45.2$^+$ spleen cells (middle histograms) and B220$^+$ CD23^{bright}-gated CD45.2$^+$ spleen cells (bottom histograms). Numbers in the gates show the percentage mean within CD45.2$^+$B220$^+$ cells of the following populations: top histograms, IgD$^+$ recirculating B cells (A: n = 3, $p < 0.01$; B: n = 4, $p < 0.01$); middle histograms, CD21^{bright}CD23$^+$ marginal zone B cells (A: n = 3, $p < 0.01$; B: n = 4, $p = 0.03$); and bottom histograms, CD21$^+$CD23^{bright}CD93$^-$ follicular B cells (A: n = 3, $p < 0.01$; B: n = 4, $p < 0.01$) and CD21$^+$CD23^{bright}CD93$^+$ transitional B cells (A: n = 3, $p < 0.01$; B: n = 4, $p < 0.01$). Total numbers, means, and standard deviations of the indicated cell subsets in the mixed chimeras are shown in Table S2. See also Figure S2.

16 ± 7.3%), and the percentage of FO B cells (CD21$^+$ CD23^{bright}CD93$^-$) was decreased (24.1% ± 8.6% versus 60.4% ± 3.2%) (Figures 1E and 1F). This effect was accompanied by an overrepresentation of MZ B cells (10.8% ± 4.8% versus 20.8% ± 6.2%) (Figure 1E and Table S1) and of B1a and B1b subsets (Figures S1J and S1K). These results suggest that the absence of Dicer preferentially drives differentiation of transitional B cells into MZ B cells rather than FO B cells.

Terminal Differentiation of Transitional Cells Is Altered in Dicer-Deficient Mice

The relative contribution of different spleen B cell subsets reflected a severe drop in the absolute number of FO cells, whereas transitional and MZ B cell numbers were normal or slightly increased (Table S1). A number of mouse models with defective B cell differentiation tend to accumulate a higher proportion of MZ and B1 cells accompanying a severe defect of FO cell generation (Martin and Kearney, 2002). This phenomenon is probably due to complex homeostatic mechanisms that seemingly compensate a lymphopenic scenario by favoring the generation of a competent first-barrier defense provided by B1 and MZ cells (reviewed in Martin and Kearney, 2002). To discriminate whether the MZ versus FO bias observed in Dicer-deficient animals was due to lymphopenia-driven compensatory events or to a true requirement of microRNAs for FO B cell differentiation from transitional cells, we performed reconstitution experiments by using bone marrow mixed chimeras. We mixed wild-type CD45.1$^+$ bone marrow cells with CD45.2$^+$ cells from either *Cd19*-Cre$^{ki/+}$ *Dicer1*$^{fl/+}$ (50% *Dicer1*$^{fl/+}$) or *Cd19*-Cre$^{ki/+}$ *Dicer1*$^{fl/fl}$ (50% *Dicer1*$^{fl/fl}$) mice. Unmixed bone marrow cells from CD45.2$^+$ *Cd19*-Cre$^{ki/+}$ *Dicer1*$^{fl/+}$ (100% *Dicer1*$^{fl/+}$) and *Cd19*-Cre$^{ki/+}$ *Dicer1*$^{fl/fl}$ (100% *Dicer1*$^{fl/fl}$) mice were used as controls. Cells were transferred into lethally irradiated CD45.2$^+$ wild-type hosts, and bone marrow and spleen reconstitution was assessed after 12 weeks. At this time point, the number of CD45.2$^+$ B220$^+$ cells was <1% of normal numbers in mice that were transferred with CD45.1 cells alone, indicating that the contribution of host-derived B cell progenitors is negligible in these experiments (data not shown). As expected, we found that 100% *Dicer1*$^{fl/fl}$ reconstitution resulted in a decrease of both IgD$^+$ bone marrow and FO spleen subsets as compared to 100% *Dicer1*$^{fl/+}$ reconstituted mice, phenocopying our observations in *Cd19*-Cre$^{ki/+}$ *Dicer1*$^{fl/+}$ and *Cd19*-Cre$^{ki/+}$ *Dicer1*$^{fl/fl}$ animals (Figure 2A). CD45.1$^+$ wild-type cells alleviated the lymphopenia driven by Dicer-deficient cells, given that 50% *Dicer1*$^{fl/fl}$ mixed chimeras contained total absolute numbers of transitional, FO, and MZ cells indistinguishable from those in 50% *Dicer1*$^{fl/+}$ control chimeras (Table S2). In spite of the normal numbers of total spleen cells, we observed that CD45.2$^+$ cells in 50% *Dicer1*$^{fl/fl}$ reconstituted mice still showed an impairment of FO B cell generation (60.6% ± 3.5% versus 34.9% ± 2.6%) and an overrepresentation of the MZ compartment (8.7% ± 1.5% versus 13.8% ± 2.7%) (Figure 2B and Table S2). These results indicate that MZ overrepresentation in Dicer-deficient animals is not a homeostatic response secondary to lymphopenia, but instead reflects a skewed terminal differentiation pattern promoted by the absence of microRNAs. To rule out that this phenotype could be the result of an enhanced depletion of microRNAs taking place specifically in FO cells, we measured Dicer expression in transitional, MZ, and FO cells from *Cd19*-Cre$^{ki/+}$ *Dicer1*$^{fl/+}$ and *Cd19*-Cre$^{ki/+}$ *Dicer1*$^{fl/fl}$ spleens (Figure S2). This analysis showed that Dicer expression was lowest at the transitional stage of

Cd19-Cre$^{ki/+}$ *Dicer1*$^{fl/fl}$ spleens and that it slightly increased in mature FO cells. This result indicates that Dicer depletion does not proceed beyond the transitional stage and rather suggests that those cells retaining some Dicer expression selectively differentiate into FO cells. We conclude that Dicer depletion in late B cell differentiation results in a biased terminal differentiation of transitional cells that impairs FO cell development while favoring the generation of MZ cells.

MicroRNA Profiling in FO and MZ B Cells

To examine the microRNAs that could be functionally relevant in determining the FO versus MZ B cell fate, we performed microarray analysis and compared microRNA expression in FO and MZ B cells from *Cd19*-Cre$^{ki/+}$ *Dicer1*$^{fl/+}$ mice. FO and MZ B cells were isolated by cell sorting, and RNA was labeled and hybridized to microRNA arrays. We consistently detected expression of 177 microRNAs in FO cell samples. Statistical analysis was performed so that those microRNAs that were differentially expressed in MZ versus FO B cells could be identified ($p < 0.1$, see Experimental Procedures). This analysis showed that 31 of the 177 detected microRNAs were differentially expressed in these two subsets (Figure 3A), all of which were found to be expressed at lower amounts in FO *Cd19*-Cre$^{ki/+}$ *Dicer1*$^{fl/fl}$ than in FO *Cd19*-Cre$^{ki/+}$ *Dicer1*$^{fl/+}$ cells (not shown), as expected from the absence of Dicer. Interestingly, we found that in *Cd19*-Cre$^{ki/+}$ *Dicer1*$^{fl/+}$ control animals all 31 microRNAs were expressed at higher amounts in FO than in MZ B cells (Figure 3A). This result was validated by real-time RT-PCR for a number of microRNAs, including miR141, miR16, miR192, and miR194. In all the cases, we found that RT-PCR results confirmed that these microRNAs displayed higher expression in FO than in MZ B cells (Figure S3A). This observation accords with our finding that in *Cd19*-Cre$^{ki/+}$ *Dicer1*$^{fl/fl}$ mice MZ generation is favored over FO generation and suggests that microRNAs can be more determinant for FO than MZ B cell differentiation.

miR185 and Btk Deregulation in *Cd19*-Cre$^{ki/+}$ *Dicer1*$^{fl/fl}$ B Cells Shifts BCR Stimulation Response

To gain insights into the functional relevance of the differentially expressed microRNAs identified by array analysis, we followed a hypothesis-driven bioinformatics approach by searching for microRNAs that could target genes reported to play a role in the FO versus MZ B cell generation. In particular, we performed a prediction search using three independent software (MiRanda, miRBase, and TargetScan) by scanning all differentially expressed microRNAs for potential binding to Aiolos (gene symbol, *Ikzf3*), *Btk*, CD21 (gene symbol, *Cr2*), and *Notch2* mRNAs. We found that all three software predicted miR185 to target one such gene, *Btk* (Figure S3B), with an identical seed sequence at position 17–39 of its 3′ UTR. Btk, a kinase that transduces signals downstream of the BCR, has been shown to be involved in the generation or recruitment of autoreactive B cells to the MZ area (Martin and Kearney, 2000). Real-time PCR analysis confirmed that miR185 expression was regulated in peripheral B cell subsets, with transitional cells displaying intermediate miR185 amounts that were upregulated in FO cells and downregulated in MZ cells (Figure S3C).To test whether miR185 can be regulating Btk expression in B cells, we overexpressed miR185 in primary B cells from wild-type spleens and measured Btk expression by real-time PCR after 3 days of LPS + IL4 stimulation. We found that miR185 transduction, but not transduction of mock or an irrelevant miRNA (miR27a) vector, resulted in a decrease of Btk mRNA expression (Figure 3B, $p = 0.005$). Dicer expression itself, included as a control, was unchanged in B cells transduced with any of the three vectors (Figure 3B). Importantly, we found that Btk protein expression was increased in *Cd19*-Cre$^{ki/+}$ *Dicer1*$^{fl/fl}$ spleen B cells when compared to *Cd19*-Cre$^{ki/+}$ *Dicer1*$^{fl/+}$ counterparts (Figure 3C). Specifically, Btk expression was substantially increased in transitional and FO *Cd19*-Cre$^{ki/+}$ *Dicer1*$^{fl/fl}$ cells, whereas this difference is not evident in MZ cells, in agreement with the observed block in FO but not MZ B cell differentiation (Figure 3D). The strength of BCR signaling is critical for determining B cell fate (Grimaldi et al., 2005; Pillai and Cariappa, 2009; Shlomchik, 2008), and Btk has been reported as one of the components involved in establishing this threshold and influencing the differentiation of MZ B cells (Halcomb et al., 2008; Khan et al., 1995; Martin and Kearney, 2000; Ng et al., 2004; Satterthwaite et al., 1997). To determine whether elevated Btk expression correlated with enhanced BCR signaling in *Cd19*-Cre$^{ki/+}$ *Dicer1*$^{fl/fl}$ B cells, we examined the increase of ERK phosphorylation in *Cd19*-Cre$^{ki/+}$ *Dicer1*$^{fl/+}$ and *Cd19*-Cre$^{ki/+}$ *Dicer1*$^{fl/fl}$ B cells in response to BCR stimulation. We found that stimulation with IgM antibodies consistently resulted in a higher amount of ERK phosphorylation in Dicer-deficient B cells when compared to control cells (Figure 3E). We next addressed downstream events of BCR signaling by analyzing the efficiency of class switch recombination in B cells stimulated with anti-IgM and IL4. Consistent with the observed increase in Btk protein expression and ERK phosphorylation, *Cd19*-Cre$^{ki/+}$ *Dicer1*$^{fl/fl}$ B cells showed a higher rate of class switch recombination to IgG1 (1.5% ± 0.25% versus 3.2% ± 0.78% at 72 hr, $p = 0.03$) (Figure 3F). To address whether deregulated expression of miR185 and Btk was directly responsible for the enhanced BCR signaling phenotype, we performed gain-of-function experiments. Spleen B cells from wild-type mice were BCR stimulated with anti-IgM and IL-4, transduced with retroviruses encoding either Btk or miR185 precursor, and measured the rate of class switch recombination to IgG1. We found that Btk overexpression recapitulated the phenotype observed in *Cd19*-Cre$^{ki/+}$ *Dicer1*$^{fl/fl}$ B cells, i.e., increased the rate of class switch recombination (control, 5.3% ± 1.6%; Btk-transduced, 7.7% ± 2.1%). Conversely, miR185 overexpression resulted in a decrease of the class switch recombination efficiency (control, 5.3% ± 1.6%; miR185-transduced, 4.0% ± 1.8%) (Figure 3G). Together, these results establish a direct role of miR185 downregulation in the modulation of BCR signaling in *Cd19*-Cre$^{ki/+}$ *Dicer1*$^{fl/fl}$ B cells through the release of negative regulation of Btk and suggest that altered BCR signaling is responsible for the biased selection and commitment of *Cd19*-Cre$^{ki/+}$ *Dicer1*$^{fl/fl}$ peripheral B cells.

Cd19-Cre$^{ki/+}$ *Dicer1*$^{fl/fl}$ B Cells Express a Skewed Ig Repertoire

To determine whether the altered pattern of B cell generation and BCR signaling results in a skewed selection of the antibody repertoire in the absence of microRNAs, we examined the VDJ rearrangements of the expressed immunoglobulin heavy chains in B cells from *Cd19*-Cre$^{ki/+}$ *Dicer1*$^{fl/+}$ and *Cd19*-Cre$^{ki/+}$ *Dicer1*$^{fl/fl}$ mice. Spleen B cells were isolated and the proportion of

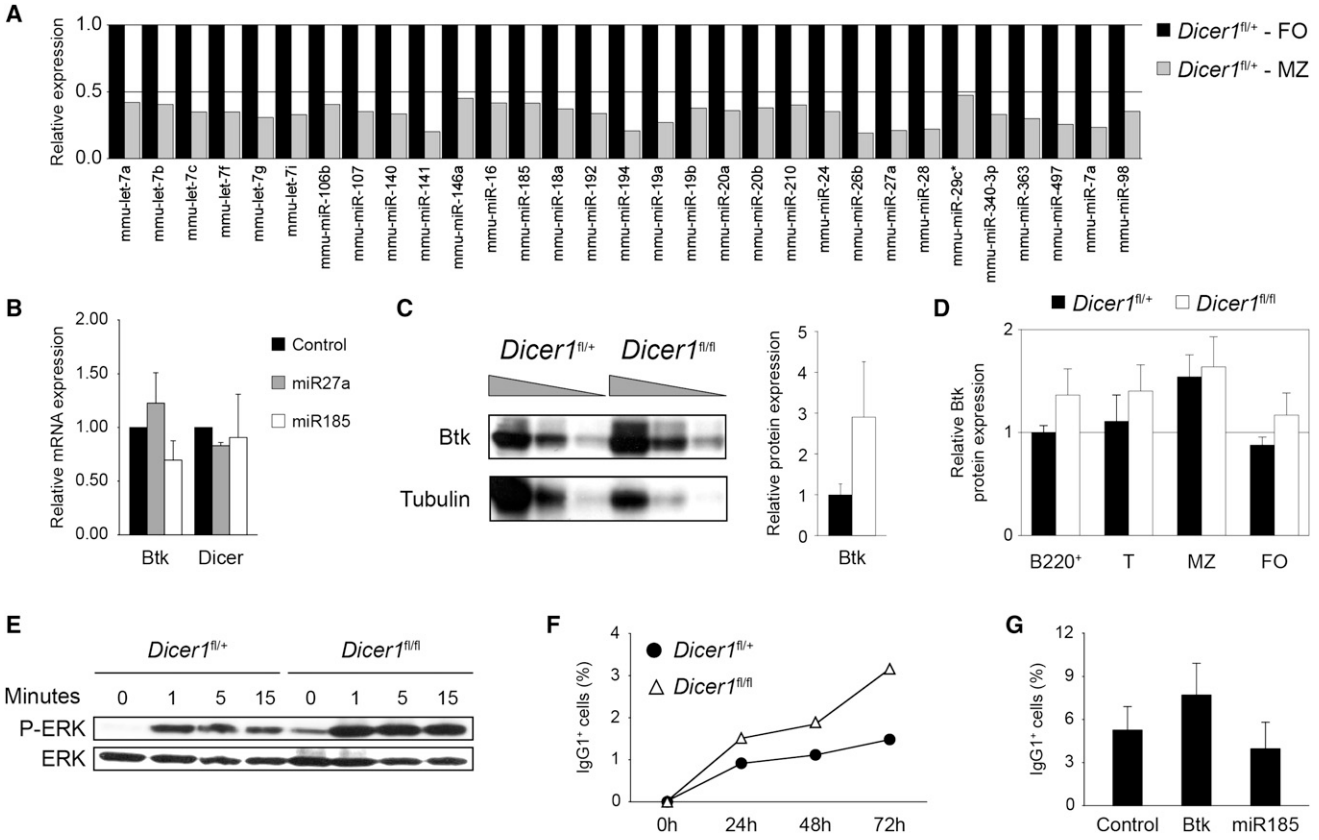

Figure 3. MicroRNA Analysis of FO and MZ B Cells and BCR Signaling Alterations in Dicer-Deficient Cells

(A) MicroRNA profiling of FO and MZ cell subsets of *Cd19*-Cre$^{ki/+}$ *Dicer1*$^{fl/+}$ mice. CD21^{+}CD23^{bright} follicular (FO) and CD21^{bright}CD23^{+} marginal zone (MZ) B cells were separated by cell sorting from *Cd19*-Cre$^{ki/+}$ *Dicer1*$^{fl/+}$ spleens. RNA was isolated, labeled, and hybridized on Agilent microRNA arrays. Differentially expressed microRNAs in MZ (gray bars) versus FO (black bars) cells (see Experimental Procedures) are shown ($p < 0.1$). Bars represent fluorescence intensity normalized to FO cells (mean values of three independent experiments).

(B) Differentially expressed microRNAs (shown in A) were subjected to target prediction analysis of genes potentially involved in MZ versus FO cell differentiation and/or maintenance. miR185 was predicted to target *Btk* by all three miRNA target prediction software used (MiRanda, TargetScan, and miRBase). Control, miR185, and miR27a (not predicted to target *Btk*) retroviral vectors were transduced into primary B cells from wild-type spleens in the presence of LPS and IL4. Two days after transduction, RNA was isolated and Btk mRNA was measured by real-time RT-PCR (control versus miR185: $n = 4$, $p < 0.01$). Dicer mRNA amounts from the same samples are shown as a negative control (control versus miR185: $n = 4$, $p = 0.73$). Bars represent mRNA amounts after normalization to GAPDH expression and relative to control-transduced cells. Standard deviations are shown.

(C) Btk protein expression is increased in spleen B cells of Dicer-deficient mice. Two-fold serial dilutions of total lysates from *Cd19*-Cre$^{ki/+}$ *Dicer1*$^{fl/+}$ and *Cd19*-Cre$^{ki/+}$ *Dicer1*$^{fl/fl}$ spleen B cells were analyzed by immunoblotting with Btk and tubulin antibodies. Densitometric quantification is shown on the right; the black bar represents *Cd19*-Cre$^{ki/+}$ *Dicer1*$^{fl/+}$ mice and the white bar represents *Cd19*-Cre$^{ki/+}$ *Dicer1*$^{fl/fl}$ mice ($n = 2$, $p < 0.01$).

(D) Btk protein expression in B cell subsets. Spleen cell suspensions from *Cd19*-Cre$^{ki/+}$ *Dicer1*$^{fl/+}$ (black bars) and *Cd19*-Cre$^{ki/+}$ *Dicer1*$^{fl/fl}$ mice (white bars) were surface stained with anti-B220, anti-CD21, anti-CD23, and anti-CD93, intracellularly stained with anti-Btk, and analyzed by flow cytometry. Mean fluorescence in the indicated subsets was normalized to *Cd19*-Cre$^{ki/+}$ *Dicer1*$^{fl/+}$ cell fluorescence in total B220^{+} cells (B220^{+}: $n = 8–10$, $p < 0.01$; T: $n = 8–10$, $p = 0.02$; MZ: $n = 8–10$, $p = 0.41$; FO: $n = 8–10$, $p < 0.01$).

(E) Increased phospho-ERK expression in *Cd19*-Cre$^{ki/+}$ *Dicer1*$^{fl/fl}$ cells. *Cd19*-Cre$^{ki/+}$ *Dicer1*$^{fl/+}$ and *Cd19*-Cre$^{ki/+}$ *Dicer1*$^{fl/fl}$ spleen B cells were stimulated with anti-IgM and total lysate from 1×10^{6} cells was loaded per lane for analyzing anti-phospho-ERK and anti-ERK protein expression by immunoblotting. Time after stimulation is indicated over each lane.

(F) Increased class switching in Dicer-deficient cells upon stimulation with anti-IgM. Spleen B cells from *Cd19*-Cre$^{ki/+}$ *Dicer1*$^{fl/+}$ (filled circles) and *Cd19*-Cre$^{ki/+}$ *Dicer1*$^{fl/fl}$ mice (triangles) were isolated and cultured in the presence of anti-IgM and IL4. The efficiency of class switch recombination to IgG1 was analyzed by flow cytometry at the indicated time points ($n = 3$).

(G) Btk and miR185 gain-of-function analysis. Wild-type spleen B cells were transduced with Btk, miR185, or empty vectors in the presence of anti-IgM and IL4. The efficiency of class switching to IgG1 was analyzed by flow cytometry 96 hr after transduction. Bars represent the percentage of IgG1^{+} cells within transduced GFP^{+} cells. Standard deviations from three independent experiments are shown ($n = 3$, $p = 0.03$). See also Figure S3.

J_H elements was determined after RT-PCR, cloning, sequencing and IgBlast analysis (Table S3 and Figure 4A). We found that the usage of J_H genes was significantly altered ($p = 0.0002$) in *Cd19*-Cre$^{ki/+}$ *Dicer1*$^{fl/fl}$ as compared to control B cells, with an overrepresentation of J_H4 segments in Dicer-deficient cells (Figure 4A). In addition, the number of R and K residues at the CDR3 region, a feature of autoreactivity (Crouzier et al., 1995; Ichiyoshi and Casali, 1994; Wardemann et al., 2003), was significantly

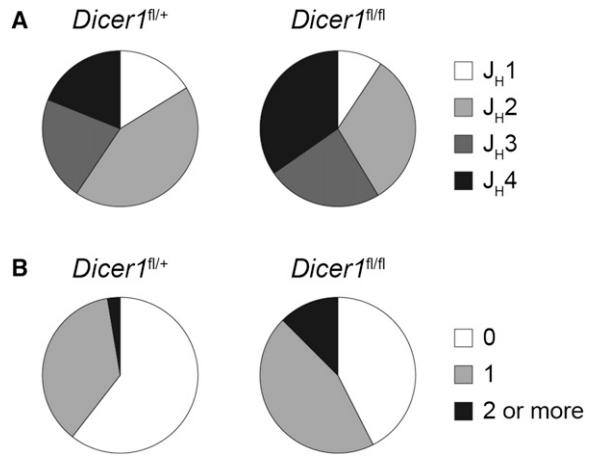

Figure 4. *Cd19*-Cre$^{ki/+}$ *Dicer1*$^{fl/fl}$ B Cells Express a Skewed Ig Repertoire

Analysis of the expressed IgH repertoire in control and Dicer-deficient B cells. B cells were isolated from *Cd19*-Cre$^{ki/+}$ *Dicer1*$^{fl/+}$ and *Cd19*-Cre$^{ki/+}$ *Dicer1*$^{fl/fl}$ spleens by immunomagnetic depletion. RNA was extracted, retrotranscribed, and PCR-amplified with oligonuclotides specific for VHJ558 or VH7183 in combination with a Cμ oligonucleotide. PCR products were cloned, sequenced, and analyzed with IgBlast software. Sectors represent the contribution of J_H segments (A) (n = 74-75, $p < 0.01$) and of sequences containing 0, 1, or ≥ 2 R+K residues at CDR3 (B) (n = 74–75, p = 0.03) for *Cd19*-Cre$^{ki/+}$ *Dicer1*$^{fl/+}$ and *Cd19*-Cre$^{ki/+}$ *Dicer1*$^{fl/fl}$ B cells. Results were pooled from four independent animals of each genotype. Complete sequence analysis is shown in Table S3.

increased (p = 0.03) in *Cd19*-Cre$^{ki/+}$ *Dicer1*$^{fl/fl}$ B cells (Figure 4B). Therefore, in the absence of Dicer there is a redistribution of variable segments in the antibody repertoire.

Cd19-Cre$^{ki/+}$ *Dicer1*$^{fl/fl}$ Females Display Autoimmune Features

The observation that microRNA-deficient B cells contain a higher number of positive charges in their Ig heavy chains prompted us to assess the autoreactivity of serum Igs from *Cd19*-Cre$^{ki/+}$ *Dicer1*$^{fl/+}$ and *Cd19*-Cre$^{ki/+}$ *Dicer1*$^{fl/fl}$ mice. Sera from *Cd19*-Cre$^{ki/+}$ *Dicer1*$^{fl/+}$ and *Cd19*-Cre$^{ki/+}$ *Dicer1*$^{fl/fl}$ animals were collected and antibody reactivity against self-antigens was measured by ELISA and compared to titers found in MRL$^{lpr/lpr}$ mice. Importantly, we found that titers of IgGs against dsDNA, ssDNA, and cardiolipin autoantigens were significantly increased in serum from aged female but not male *Cd19*-Cre$^{ki/+}$ *Dicer1*$^{fl/fl}$ mice (Figures 5A–5C). Although total IgG and IgM antibody titers were on average slightly increased in *Cd19*-Cre$^{ki/+}$ *Dicer1*$^{fl/fl}$ mice (not shown), this difference was not statistically significant and did not correlate with the autoantibody titers in individual mice (Figure S4). This suggests that accumulation of autoantibodies in the absence of Dicer is not passively correlated to higher total Ig titers, but rather is the result of a biased repertoire selection. To address the pathogenicity of autoantibodies in Dicer-deficient females, we assessed the presence of immune complexes in kidney sections. Indeed, immunoflurescence analysis revealed a prominent accumulation of IgG in *Cd19*-Cre$^{ki/+}$ *Dicer1*$^{fl/fl}$ aged females when compared to control animals (Figure 6A and Figure S5A), indicative of deposition of immune complexes. Moreover, silver-PAS staining of kidney sections showed massive lymphocyte infiltration and overall damage of glomerulus architecture that affected 50% of aged Dicer-deficient females (Figure 6B and Figure S5B). We conclude that the absence of microRNAs gives rise to a skewed antibody repertoire enriched in self-reactive specificities that leads to the development of autoimmune disease.

DISCUSSION

In this study, we have addressed the role of microRNAs in terminal B cell differentiation by analyzing *Cd19*-Cre$^{ki/+}$ *Dicer1*$^{fl/fl}$ mice. Although CD19 expression and Dicer deletion could be expected to take place at the pre-B stage of bone marrow development (Rickert et al., 1997), we found that the expression of Dicer mRNA is substantially decreased only in bone marrow IgM$^+$ cells. This late depletion, which probably reflects a gradual deletion during bone marrow differentiation (Hobeika et al., 2006) together with a high stability of Dicer mRNA, allowed the generation of mature B cells and their migration to peripheral tissues. Indeed, the sharpest reduction in Dicer expression was observed in spleen transitional cells. We found here that in the absence of Dicer, normal numbers of transitional B cells are

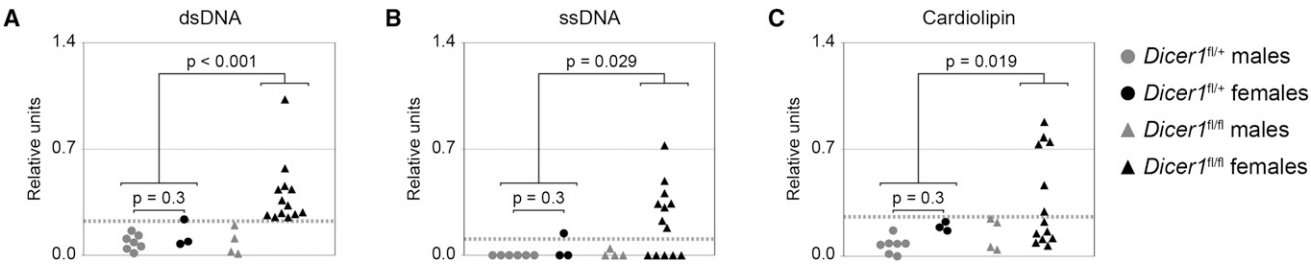

Figure 5. *Cd19*-Cre$^{ki/+}$ *Dicer1*$^{fl/fl}$ Mice Have High Serum Titers of Autoreactive Antibodies

Analysis of serum Ig titers against self-antigens. Serum from 40- to 60-week-old *Cd19*-Cre$^{ki/+}$ *Dicer1*$^{fl/+}$ (circles) and *Cd19*-Cre$^{ki/+}$ *Dicer1*$^{fl/fl}$ (triangles) animals was collected and reactivity against dsDNA (A), ssDNA (B), and cardiolipin (C) was assessed by ELISA. The results are represented as relative colorimetric units. Background signal from RAG knockout mouse serum was subtracted and values were normalized to the signal obtained from MRL$^{lpr/lpr}$ mouse serum. For clarity, results obtained from males (gray) and females (black) are represented separately. A threshold for autoreactive antibody titers was established by addition of two standard deviations to the mean value of the titers detected in the control *Cd19*-Cre$^{ki/+}$ *Dicer1*$^{fl/+}$ mice (shown as a gray dotted line). p values (Fisher's exact test) between the indicated groups are shown (n = 9–17). See also Figure S4.

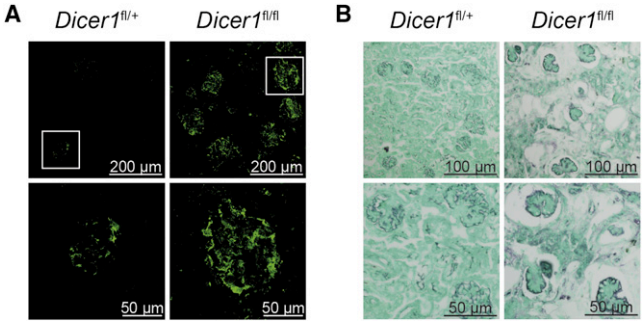

Figure 6. *Cd19*-Cre$^{ki/+}$ *Dicer1*$^{fl/fl}$ Females Display Autoimmune Features

(A) Immunocomplexes in kidneys from Dicer-deficient females. Kidney sections from 40- to 60-week-old *Cd19*-Cre$^{ki/+}$ *Dicer1*$^{fl/+}$ and *Cd19*-Cre$^{ki/+}$ *Dicer1*$^{fl/fl}$ animals were stained with anti-IgG. Representative immunofluorescence glomerular stainings are shown at two different magnifications. Scale bars are indicated.

(B) Kidney damage in *Cd19*-Cre$^{ki/+}$ *Dicer1*$^{fl/fl}$ mice. Formalin-fixed kidney sections from *Cd19*-Cre$^{ki/+}$ *Dicer1*$^{fl/+}$ and *Cd19*-Cre$^{ki/+}$ *Dicer1*$^{fl/fl}$ aged mice were subjected to Silver-PAS staining. Scale bars are shown. See also Figure S5.

generated, which can differentiate normally into MZ B cells; in contrast, the generation of FO B cells is severely compromised. Interestingly, this biased differentiation is cell autonomous, which indicates that microRNAs are critical for MZ versus FO cell fate determination. In this regard, we provide in this study the first analysis of microRNA expression in MZ versus FO B cells. Notably, we found that only a relatively reduced number of microRNAs are differentially expressed in MZ versus FO cells, all of which display a higher expression amount in the latter population. This global overexpression of microRNAs in the FO subset could in turn be related to the higher Dicer expression found in FO cells as compared with transitional or MZ B cells. Differential Dicer expression in these B cell subsets is a somehow unexpected result that deserves further investigation. Regardless of the regulatory mechanism responsible for this expression pattern, this microRNA profiling can open new perspectives on the study of the developmental program that determines the selective mechanisms operating at transitional B cells and their final commitment into MZ and FO subsets.

A number of findings presented here support the idea that FO B cell generation has a deeper dependency on microRNA expression: (1) Dicer-deficient B cell progenitors give rise to normal numbers of transitional and MZ cells but to severely reduced numbers of FO cells, as measured in *Cd19*-Cre$^{ki/+}$ *Dicer1*$^{fl/fl}$ animals, bone marrow transfers and competitive bone marrow chimeras; (2) in wild-type animals, differentially expressed microRNAs show higher expression in FO than in MZ; and (3) the few FO cells that are generated in *Cd19*-Cre$^{ki/+}$ *Dicer1*$^{fl/fl}$ mice express higher amounts of Dicer than their immediate precursors, transitional cells, suggesting that only cells where Dicer depletion is incomplete—i.e., deletion of a single allele—selectively differentiate into the FO cell lineage.

Btk is known to influence the MZ versus FO cell lineage decision, and we report here that miR185 negatively regulates the expression of Btk in primary B cells. We show that miR185 expression is regulated during terminal B cell differentiation, with intermediate amounts at the transitional stage that become downregulated in MZ B cells and upregulated in FO cells. Importantly, this expression pattern mirrors that of Btk expression, which suggests that greater Btk amounts are more compatible with the generation of MZ B cells and suggests a link between the skewed generation of MZ and FO cells observed in Dicer-deficient animals and an altered BCR signaling. We show that this is indeed the case. Dicer-deficient B cells contain higher amounts of Btk protein and ERK phosphorylation and they undergo class switch recombination in response to BCR stimulation at a higher rate than control animals. This effect is phenocopied by Btk overexpression and counterbalanced by miR185 overexpression. Therefore, although other molecular pathways can play a role in the observed phenotype in *Cd19*-Cre$^{ki/+}$ *Dicer1*$^{fl/fl}$ mice, our data provide evidence that miR185 and Btk contribute to determining B cell fate by influencing the outcome of BCR signaling.

This notion is further reinforced by the finding that the Ig repertoire expressed by peripheral B cells is skewed in these animals. This observation could be explained by a shifted usage of J_H segments during V(D)J recombination or by an abnormal selection of the Ig repertoire. However, given that major Dicer mRNA depletion is first observed in immature IgM$^+$ cells, the first possibility is very unlikely and our results rather support the view that in Dicer-deficient B cells, the establishment of tolerance is incomplete. Our data suggest that Dicer deficiency results in lower amounts of miR185 and accumulation of Btk, which in turn can allow the selection of B cells bearing self-reactive BCRs and favor the final commitment of some of these cells into a MZ fate. This hypothesis is compatible with the observation that relatively subtle changes in Btk expression and/or activity influence the generation of MZ and FO cells (Dingjan et al., 1998; Maas et al., 1999) and could explain the observed accumulation of serum autoantibodies and the presence of features of autoimmune disease in aged Dicer-deficient animals.

Interestingly, the autoimmune disease observed in Dicer-deficient animals was predominantly found in female rather than male mice, very much resembling the profound prevalence of female incidence in various autoimmune diseases in humans, such as systemic lupus erythematosus, Sjoegren's syndrome, or scleroderma (Whitacre, 2001). Therefore, we envision that the analysis of microRNA expression profiles can prove clinically useful in the diagnosis and prognosis of autoimmune disease. In summary, our data provide evidence on the role of microRNAs in maintaining a tolerant antibody repertoire and will contribute a new perspective on gender-biased autoimmune syndromes by allowing the study of microRNA-based gene regulation under differential hormone contexts.

EXPERIMENTAL PROCEDURES

Mice

B cell-specific Dicer-deficient (*Cd19*-Cre$^{ki/+}$ *Dicer1*$^{fl/fl}$) and littermate control (*Cd19*-Cre$^{ki/+}$ *Dicer1*$^{fl/+}$) mice were generated by breeding *Dicer1*$^{fl/fl}$ to *Cd19*-Cre$^{ki/+}$ (Harfe et al., 2005; Rickert et al., 1997) mice. All mice were housed under pathogen-free conditions in accordance with the recommendations of the Federation of European Laboratory Animal Science Associations. All experiments were performed following the Animal Bioethics and Comfort Committee protocols approved by the Instituto de Salud Carlos III.

Flow Cytometry

Cells from bone marrow and spleen were collected and erythrocytes were lysed with ACK Lysing Buffer (BioWhittaker). Then, cells were cell surface-stained with different combinations of anti-mouse Btk, IgM, IgD, IgG1, Mac-1, CD3, CD4, CD5, CD21, CD23, CD25, CD43, and CD45.2 (BD Biosciences) and anti-B220 (Miltenyi Biotec) and anti-CD93 (eBioscience). For Btk intracellular staining, extracellular marked cells were fixed with PFA and permeabilized with 0.05% saponin and stained with Btk antibody in 1× PBS-0.05% saponin. Flow cytometry analyses were performed in a FACSCanto flow cytometer with FACSDiva (BD Biosciences) or FlowJo (Tree Star) softwares.

Bone Marrow Reconstitution

A total of 5 × 10^6 total bone marrow cells from CD45.1 C57BL/6, CD45.2 *Cd19*-Cre$^{ki/+}$ *Dicer1*$^{fl/+}$, or CD45.2 *Cd19*-Cre$^{ki/+}$ *Dicer1*$^{fl/fl}$ donor mice were injected intravenously into 8- to 12-week-old CD45.2 C57BL/6 mice that had been lethally irradiated (2 × 550 cGy) 24 hr before the reconstitution. For competitive bone marrow reconstitutions, mice were injected with cell mixtures containing 2.5 × 10^6 bone marrow cells from CD45.1 C57BL/6 mice and 2.5 × 10^6 bone marrow cells from CD45.2 *Cd19*-Cre$^{ki/+}$ *Dicer1*$^{fl/+}$ or *Cd19*-Cre$^{ki/+}$ *Dicer1*$^{fl/fl}$ mice. Chimeric mice were analyzed 12 weeks after the reconstitution.

Cell Cultures

293T cells were cultured in DMEM supplemented with 10% FCS. Primary spleen B cells were purified from spleens by immunomagnetic depletion with anti-CD43 beads (Miltenyi Biotec) and cultured in RPMI 1640 supplemented with 10% FCS, 10 mM HEPES (Invitrogen), and 50 μM β-mercaptoethanol (Invitrogen). For Btk expression analysis upon miRNA overexpression, 25 μg/mL LPS (Sigma-Aldrich) and 10 ng/mL IL4 (PeproTech) were added to the medium. For class switch recombination analysis, 10 μg/mL F(ab)'$_2$ fragments of goat anti-mouse IgM (Jackson Immunoresearch) and 10 ng/mL IL4 (PeproTech) were added to the medium.

Retroviral Infection

Retroviral supernatants were produced by transient calcium phosphate cotransfection of NIH-293T cells with pCL-Eco (Imgenex) and pre-miRNA-GFP retroviral vectors or pMXPIE-Btk retroviral vector. pre-miRNA-GFP vectors encoded pre-miRNA (pre-miR27a or pre-miR185) and their flanking 50-bp-long genomic sequences (de Yébenes et al., 2008). Mouse primary B cells were transduced with retroviral supernatants for 20 hr in the presence of 8 μg/ml polybrene (Sigma), 10 mM HEPES (Invitrogen), and 50 μM β-mercaptoethanol (Invitrogen). For Btk expression analysis upon miRNA overexpression, 25 μg/ml LPS (Sigma) and 10 ng/ml IL-4 (Peprotech) were added to the retroviral supernatants. GFP-positive cells were sorted 48 hr after transduction (FACSAria, BD Biosciences). For class switch recombination analysis upon Btk or miR185 overexpression, 10 μg/mL F(ab)'$_2$ fragments of goat anti-mouse IgM (Jackson Immunoreserach) and 10 ng/mL IL4 (PeproTech) were added to the retroviral supernatant. Ninety-six hours after transduction, IgG1 expression in GFP-positive cells was determined by flow cytometry.

miRNA Microarrays

Spleen cells from *Cd19*-Cre$^{ki/+}$ *Dicer1*$^{fl/+}$ and *Cd19*-Cre$^{ki/+}$ *Dicer1*$^{fl/fl}$ mice were stained with anti-B220, anti-CD21, and anti-CD23 as described above. B220$^+$ CD21^{bright}CD23$^+$ (marginal zone) and B220$^+$CD21$^+$CD23^{bright} (follicular) B cell populations were sorted (FACSAria, BD Biosciences) and total RNA of purified populations was extracted with TRIzol (Invitrogen) in accordance with the manufacturer's instructions. miRNA microarray hybridations were performed on mouse miRNA Microarray platform (Agilent Technologies). Local background was subtracted from median signal and intensity was transformed to a $\log_2$ scale. Normalized data were analyzed with MultiExperiment Viewer software. First, paired t test was used for determining differentially expressed miRNAs in MZ versus FO control (*Cd19*-Cre$^{ki/+}$ *Dicer1*$^{fl/+}$) cells. miRNAs with a p value $\leq$ 0.1 and fold-expression difference $\geq$2 were selected for further analysis. Then control (*Cd19*-Cre$^{ki/+}$ *Dicer1*$^{fl/+}$) and Dicer-deficient (*Cd19*-Cre$^{ki/+}$ *Dicer1*$^{fl/fl}$) cells were compared with an unpaired t test for both MZ and FO cell subsets. Again, miRNAs with a p value $\leq$ 0.1 and fold-expression difference $\geq$ 2 were selected. Thirty-one miRNAs were identified in FO-control versus Dicer-deficient analysis and only four were identified in MZ-control versus Dicer-deficient analysis, all of which were contained in the FO analysis results.

Real-Time PCR

B cell populations were sorted from spleen or bone marrow after staining with B220, IgM, CD21, CD23, and CD93 antibodies. T regulatory cells were isolated (>90% purity) with the CD4$^+$CD25$^+$ Regulatory T Cell Isolation Kit (Miltenyi Biotec). Total RNA was extracted with TRIzol (Invitrogen) and converted into cDNA with random hexamers (Roche) and SuperScript II reverse transcriptase (Invitrogen). Mouse Dicer and Btk mRNA were quantified with SYBR green assay (Applied Biosystems). GAPDH amplifications were used as normalization controls. The following primers were used: Dicer (forward): 5′ -ACGAAA TGCAAGGAATGGACTC-3′; Dicer (reverse): 5′-GGCACCAGCAAGAGACTC AAA-3′; Btk (forward): 5′-AGCGCTCCCAGCAGAAAAA-3′; Btk (reverse): 5′-CT TACTGCCTCTTCTCCCACG-3′; GAPDH (forward): 5′-TGAAGCAGGCATCTGA GGG-3′; GAPDH (reverse): 5′-CGAAGGTGGAAGAGTGGGAG-3′. For mature miRNA expression analysis, total RNA was extracted as previously described. Retrotranscription and real-time PCR were performed with TaqMan MicroRNA Assays (Applied Biosystems) in accordance with recommendations of the manufacturer. Amplification of sno142 was used as a normalization control.

Immunoblotting

Spleen B cells from *Cd19*-Cre$^{ki/+}$ *Dicer1*$^{fl/+}$ and *Cd19*-Cre$^{ki/+}$ *Dicer1*$^{fl/fl}$ mice were purified by immunomagnetic depletion as described above. For Btk immunoblotting, cell pellets were incubated on ice for 20 min in lysis buffer containing 20 mM Tris, 150 mM NaCl, 1% Nonidet P-40 in the presence of protease inhibitors (Roche) and lysates were cleared by centrifugation. For phospho-ERK and ERK immunoblotting, cells were incubated for 1 hr at 37°C in starvation buffer (RPMI 1640, 10 mM HEPES, and 50 μM β-mercaptoethanol) prior to stimulation with 10 μg/mL F(ab)'$_2$ fragments of goat anti-mouse IgM (Jackson Immunoreserach). Cells were pelleted after the indicated times and lysed on ice for 30 min in lysis buffer containing 50 mM Tris-HCl (pH 7.4), 1% Nonidet P-40, 137.5 mM NaCl, and 1% glycerol in the presence of protease inhibitors (Roche) and phosphatase inhibitors (NaV and NaF). Lysates were cleared by centrifugation at 4°C for 15 min at 16000 × g and 5% β-mercaptoethanol was added.

Total protein was sized-fractioned by SDS-PAGE on 10% acrylamide-bisacrylamide gel and transferred to Protran nitrocellulose membrane (Whatman) in transfer buffer (0.19 M glycine, 25 mM Tris base, and 0.01% SDS) containing 20% methanol. Gels were transferred for 1 hr at 0.4A for Btk and 2 hr at 0.2A for phospho-ERK/ERK immunoblot. Membranes were probed with anti-mouse-Btk (Abcam) and anti-mouse-Tubulin (Sigma-Aldrich) and anti-mouse-phospho-ERK (Cell Signaling) and anti-mouse-ERK (Biosource), respectively. Then, membranes were incubated with corresponding secondary HRP-conjugated antibodies (Dako) and developed with SuperSignal West Dura Extended Duration Substrate (Thermo Scientific).

Amplification and Analysis of V(D)J Rearrangements

Spleen B cells from *Cd19*-Cre$^{ki/+}$ *Dicer1*$^{fl/+}$ and *Cd19*-Cre$^{ki/+}$ *Dicer1*$^{fl/fl}$ mice were purified and total RNA was extracted and converted into cDNA as described above. IgH rearrangments were amplified from RT-PCR products with 2.5 U of Taq DNA polymerase (Roche) and combining a 3′ primer for Cμ exon 1 with a 5′ primer for V_H7183 or V_HJ558. Amplification consisted of 30 cycles (30'' at 94°C, 30'' at 57°C, and 60'' at 72°C) followed by a 10 min incubation at 72°C. PCR products were cloned into the pGEM-T Easy vector (Promega). Clones were selected randomly and sequenced with T7 universal primer. Sequences were analyzed with the NCBI IgBlast program (http://www.ncbi.nlm.nih.gov/igblast/). Cμ: 5′-ATTTGGGAAGGACTGACTCT-3′; V_H7183: 5′-GAGTCTGGGGGAGCTTA-3′; V_HJ558: 5′- RGCCTGGGRCTTC AGTGAAG-3′ (R = A or G).

ELISA

Quantification of IgG and IgM autoantibodies recognizing DNA and cardiolipin was performed by ELISA. For DNA antibodies quantification, MaxiSorp Immuno plates (Nunc) were incubated with 50 μg/mL poly-L-lysine (Sigma-Aldrich) for 2 hr at 37°C, then rinsed with water and coated with 100 μl of 2 μg/mL calf thymus DNA (Sigma-Aldrich) in phosphate-buffered saline

(1× PBS, 0.14 M NaCl, and 0.01 M NaH_2PO_4) at 4°C overnight. Single-stranded DNA was obtained by boiling DNA for 10 min and snap-chilling on ice. For cardiolipin antibody detection, plates were coated with 100 μl of 20 μg/mL cardiolipin in ethanol at 4°C overnight. Coated plates were blocked with 4% BSA PBS for 90 min at RT and washed with 0.05% Tween 20 in PBS. Sera were diluted in 1% BSA PBS, 1:500 for IgG DNA antibodies and 1:100 for IgM DNA and IgG cardiolipin antibodies detection. Fifty microliters of the dilutions were applied and incubated for 2 hr at RT. Plates were washed again and autoantibodies were detected with anti-mouse-κ/λ-chains-POD conjugates (Mouse IgG ELISA Kit, Roche) or goat anti-mouse IgM HRP-conjugated antibody (Bethyl laboratories) and then with SuperSignal ELISA Femto Maximum Sensitivity Substrate (Thermo Scientific). The OD_{425nm} was determined with a conventional microplate reader. Serum from $MRL^{lpr/lpr}$ and RAG2 knockout mice were used as positive and negative controls, respectively. The relative binding capacity to DNA or cardiolipin was calculated by subtracting background signal from RAG2 knockout serum and normalizing to $MRL^{lpr/lpr}$ signal. For determination of serum total Ig titers, Mouse IgG ELISA Kit (Roche) and Mouse IgM ELISA Quantitation Kit (Bethyl laboratoires) were used in accordance with the manufacturer's instructions.

Immunofluorescence

Kidneys were embedded on OCT compound (Tissue Tek, Sakura) and snap-frozen on dry ice. Ten micrometer sections were cut and fixed in chilled acetone for 10 min. Sections were washed with PBS, blocked for 30 min with blocking buffer (PBS, 1% BSA, 0.3% Triton, 0.5% goat serum, 0.5% donkey serum, and 1% gelatin), stained with Alexa Fluor 488 donkey anti-mouse IgG (Invitrogen), and analyzed in a Leica TCS-SP5 (AOBS) confocal microscope with a 20× HC PL APO 0.7 N.A. oil immersion objective with LAS AF software. The background was subtracted from mean fluorescence intensity of each glomerulus and obtained values were normalized for control of the mean.

Histopathology

Kidneys were fixed in 10% buffered formalin and embedded in paraffin. Sections were stained with silver methenamine P.A.S.M. in accordance with standard protocols.

Statistical Analysis

Bone marrow, spleen, and lymph nodes phenotypes, relative Dicer and Btk mRNA and protein expression, and glomerulus fluorescence intensities were analyzed with Student's t tests. Sequence analyses were performed with two-tailed Chi-square tests. For autoantibody ELISAs, a threshold was established for each particular antigen (mean of *Cd19*-$Cre^{ki/+}$ *Dicer1*$^{fl/+}$ mice serum signals plus two standard deviations). Sera with signals above this threshold were considered autoreactive and Fisher's exact test was performed. For renal damage measurement, the number of affected glomeruli was analyzed with Fisher's exact test. Statistical analyses were carried out with GraphPad software. The level of statistical significance was preset at $p < 0.05$.

ACCESSION NUMBERS

The microarray data are available in the Gene Expression Omnibus (GEO) database (http://www.ncbi.nlm.nih.gov/gds) under the accession number GSE25139.

SUPPLEMENTAL INFORMATION

Supplemental Information includes five figures and three tables and can be found with this article online at doi:10.1016/j.immuni.2010.11.010.

ACKNOWLEDGMENTS

We would like to thank C.J. Tabin and K. Rajewsky for kindly providing us with *Dicer1*$^{fl/fl}$ and *Cd19*-$Cre^{Ki/+}$ mice, respectively, V. Barreto, O. Fernandez-Capetillo, I. Moreno de Alborán, and T. Wossning for critical reading of the manuscript, and J.M. Ligos, S. Minguet, D.G. Pisano, G. Gómez, D. Megías, O. Domínguez, D. Martínez, M. Cañamero, and C. Velasco for technical advice. L.B. is supported by the Spanish National Cancer Research Center (CNIO), V.G.Y. is a Ramón y Cajal Investigator (Ministerio de Ciencia e Innovación), and A.R.R. is funded by CNIO. This work was funded by grants from Ministerio de Ciencia e Innovación (SAF2007-63130), Comunidad Autónoma de Madrid (DIFHEMAT-CM), and European Research Council Starting Grant program (BCLYM-207844).

Received: February 9, 2010
Revised: May 14, 2010
Accepted: September 8, 2010
Published online: November 18, 2010

REFERENCES

Allman, D., and Pillai, S. (2008). Peripheral B cell subsets. Curr. Opin. Immunol. *20*, 149–157.

Bassing, C.H., Swat, W., and Alt, F.W. (2002). The mechanism and regulation of chromosomal V(D)J recombination. Cell Suppl. *109*, S45–S55.

Carsetti, R., Rosado, M.M., and Wardmann, H. (2004). Peripheral development of B cells in mouse and man. Immunol. Rev. *197*, 179–191.

Crouzier, R., Martin, T., and Pasquali, J.L. (1995). Heavy chain variable region, light chain variable region, and heavy chain CDR3 influences on the mono- and polyreactivity and on the affinity of human monoclonal rheumatoid factors. J. Immunol. *154*, 4526–4535.

Dammers, P.M., Visser, A., Popa, E.R., Nieuwenhuis, P., and Kroese, F.G. (2000). Most marginal zone B cells in rat express germline encoded Ig VH genes and are ligand selected. J. Immunol. *165*, 6156–6169.

de Yébenes, V.G., Belver, L., Pisano, D.G., González, S., Villasante, A., Croce, C., He, L., and Ramiro, A.R. (2008). miR-181b negatively regulates activation-induced cytidine deaminase in B cells. J. Exp. Med. *205*, 2199–2206.

Dingjan, G.M., Maas, A., Nawijn, M.C., Smit, L., Voerman, J.S., Grosveld, F., and Hendriks, R.W. (1998). Severe B cell deficiency and disrupted splenic architecture in transgenic mice expressing the E41K mutated form of Bruton's tyrosine kinase. EMBO J. *17*, 5309–5320.

Goodnow, C.C., Crosbie, J., Adelstein, S., Lavoie, T.B., Smith-Gill, S.J., Brink, R.A., Pritchard-Briscoe, H., Wotherspoon, J.S., Loblay, R.H., Raphael, K., et al. (1988). Altered immunoglobulin expression and functional silencing of self-reactive B lymphocytes in transgenic mice. Nature *334*, 676–682.

Grimaldi, C.M., Hicks, R., and Diamond, B. (2005). B cell selection and susceptibility to autoimmunity. J. Immunol. *174*, 1775–1781.

Gu, H., Tarlinton, D., Müller, W., Rajewsky, K., and Förster, I. (1991). Most peripheral B cells in mice are ligand selected. J. Exp. Med. *173*, 1357–1371.

Halcomb, K.E., Musuka, S., Gutierrez, T., Wright, H.L., and Satterthwaite, A.B. (2008). Btk regulates localization, in vivo activation, and class switching of anti-DNA B cells. Mol. Immunol. *46*, 233–241.

Harfe, B.D., McManus, M.T., Mansfield, J.H., Hornstein, E., and Tabin, C.J. (2005). The RNaseIII enzyme Dicer is required for morphogenesis but not patterning of the vertebrate limb. Proc. Natl. Acad. Sci. USA *102*, 10898–10903.

Hartley, S.B., Crosbie, J., Brink, R., Kantor, A.B., Basten, A., and Goodnow, C.C. (1991). Elimination from peripheral lymphoid tissues of self-reactive B lymphocytes recognizing membrane-bound antigens. Nature *353*, 765–769.

Hayakawa, K., Hardy, R.R., Honda, M., Herzenberg, L.A., Steinberg, A.D., and Herzenberg, L.A. (1984). Ly-1 B cells: Functionally distinct lymphocytes that secrete IgM autoantibodies. Proc. Natl. Acad. Sci. USA *81*, 2494–2498.

Hobeika, E., Thiemann, S., Storch, B., Jumaa, H., Nielsen, P.J., Pelanda, R., and Reth, M. (2006). Testing gene function early in the B cell lineage in mb1-cre mice. Proc. Natl. Acad. Sci. USA *103*, 13789–13794.

Ichiyoshi, Y., and Casali, P. (1994). Analysis of the structural correlates for antibody polyreactivity by multiple reassortments of chimeric human immunoglobulin heavy and light chain V segments. J. Exp. Med. *180*, 885–895.

Khan, W.N., Alt, F.W., Gerstein, R.M., Malynn, B.A., Larsson, I., Rathbun, G., Davidson, L., Müller, S., Kantor, A.B., Herzenberg, L.A., et al. (1995).

Defective B cell development and function in Btk-deficient mice. Immunity *3*, 283–299.

Kim, V.N., Han, J., and Siomi, M.C. (2009). Biogenesis of small RNAs in animals. Nat. Rev. Mol. Cell Biol. *10*, 126–139.

Koralov, S.B., Muljo, S.A., Galler, G.R., Krek, A., Chakraborty, T., Kanellopoulou, C., Jensen, K., Cobb, B.S., Merkenschlager, M., Rajewsky, N., and Rajewsky, K. (2008). Dicer ablation affects antibody diversity and cell survival in the B lymphocyte lineage. Cell *132*, 860–874.

Li, Y., Li, H., and Weigert, M. (2002). Autoreactive B cells in the marginal zone that express dual receptors. J. Exp. Med. *195*, 181–188.

Maas, A., Dingjan, G.M., Grosveld, F., and Hendriks, R.W. (1999). Early arrest in B cell development in transgenic mice that express the E41K Bruton's tyrosine kinase mutant under the control of the CD19 promoter region. J. Immunol. *162*, 6526–6533.

Martin, F., and Kearney, J.F. (2000). Positive selection from newly formed to marginal zone B cells depends on the rate of clonal production, CD19, and btk. Immunity *12*, 39–49.

Martin, F., and Kearney, J.F. (2002). Marginal-zone B cells. Nat. Rev. Immunol. *2*, 323–335.

Martin, F., Oliver, A.M., and Kearney, J.F. (2001). Marginal zone and B1 B cells unite in the early response against T-independent blood-borne particulate antigens. Immunity *14*, 617–629.

Martinez, J., and Busslinger, M. (2007). Life beyond cleavage: The case of Ago2 and hematopoiesis. Genes Dev. *21*, 1983–1988.

Meffre, E., and Wardemann, H. (2008). B-cell tolerance checkpoints in health and autoimmunity. Curr. Opin. Immunol. *20*, 632–638.

Meffre, E., Casellas, R., and Nussenzweig, M.C. (2000). Antibody regulation of B cell development. Nat. Immunol. *1*, 379–385.

Nemazee, D.A., and Bürki, K. (1989). Clonal deletion of B lymphocytes in a transgenic mouse bearing anti-MHC class I antibody genes. Nature *337*, 562–566.

Ng, Y.S., Wardemann, H., Chelnis, J., Cunningham-Rundles, C., and Meffre, E. (2004). Bruton's tyrosine kinase is essential for human B cell tolerance. J. Exp. Med. *200*, 927–934.

Pillai, S., and Cariappa, A. (2009). The follicular versus marginal zone B lymphocyte cell fate decision. Nat. Rev. Immunol. *9*, 767–777.

Rickert, R.C., Roes, J., and Rajewsky, K. (1997). B lymphocyte-specific, Cre-mediated mutagenesis in mice. Nucleic Acids Res. *25*, 1317–1318.

Satterthwaite, A.B., Cheroutre, H., Khan, W.N., Sideras, P., and Witte, O.N. (1997). Btk dosage determines sensitivity to B cell antigen receptor cross-linking. Proc. Natl. Acad. Sci. USA *94*, 13152–13157.

Schmidt-Supprian, M., and Rajewsky, K. (2007). Vagaries of conditional gene targeting. Nat. Immunol. *8*, 665–668.

Shlomchik, M.J. (2008). Sites and stages of autoreactive B cell activation and regulation. Immunity *28*, 18–28.

Su, T.T., Guo, B., Wei, B., Braun, J., and Rawlings, D.J. (2004). Signaling in transitional type 2 B cells is critical for peripheral B-cell development. Immunol. Rev. *197*, 161–178.

Wardemann, H., and Nussenzweig, M.C. (2007). B-cell self-tolerance in humans. Adv. Immunol. *95*, 83–110.

Wardemann, H., Yurasov, S., Schaefer, A., Young, J.W., Meffre, E., and Nussenzweig, M.C. (2003). Predominant autoantibody production by early human B cell precursors. Science *301*, 1374–1377.

Whitacre, C.C. (2001). Sex differences in autoimmune disease. Nat. Immunol. *2*, 777–780.

Xiao, C., and Rajewsky, K. (2009). MicroRNA control in the immune system: Basic principles. Cell *136*, 26–36.

Immunity, Volume *33*

Supplemental Information

MicroRNAs Prevent the Generation of Autoreactive Antibodies

Laura Belver, Virginia G. de Yébenes, and Almudena R. Ramiro

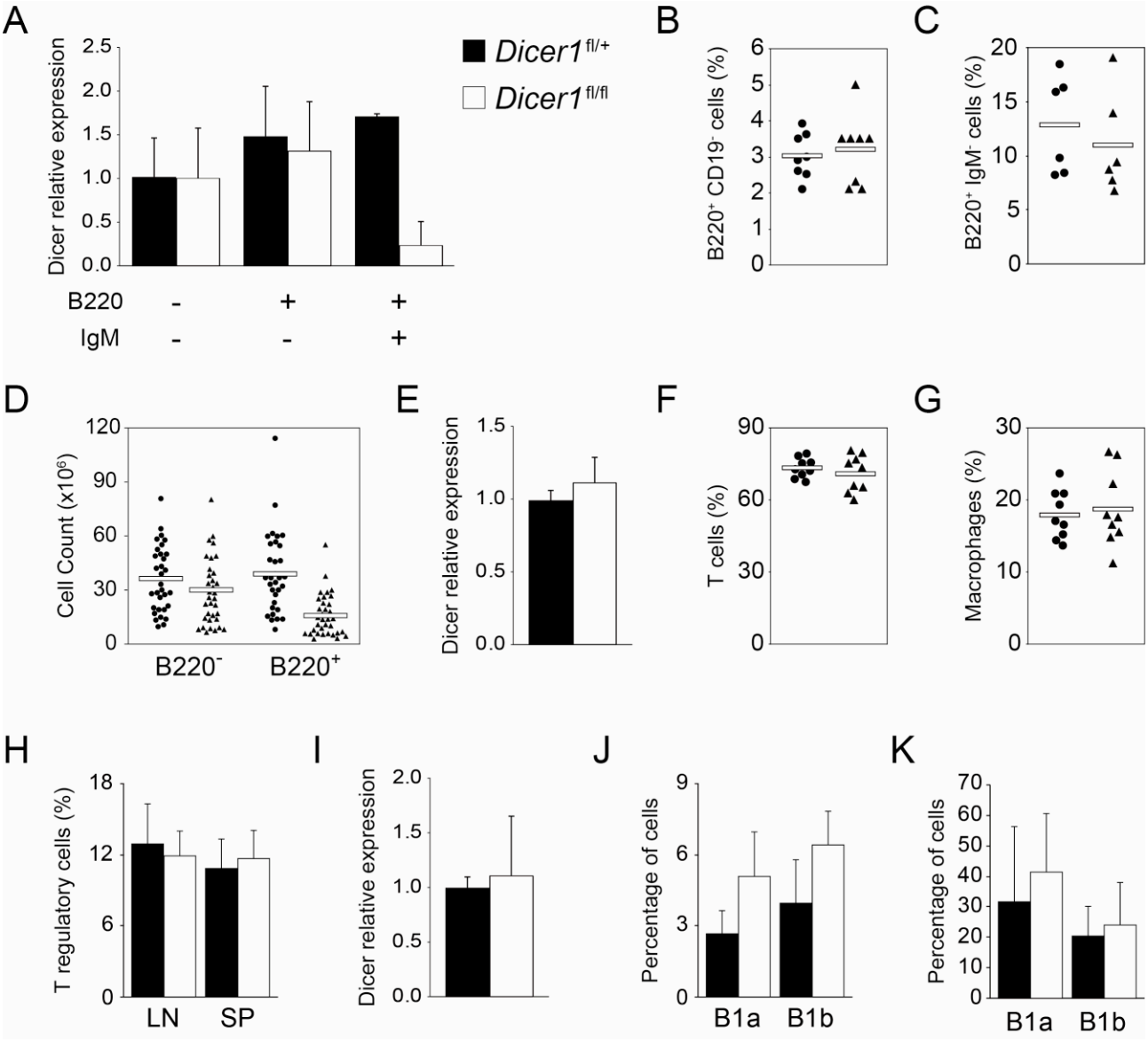

Figure S1, related to Figure 1. Phenotypic analysis of *Cd19*-Cre$^{ki/+}$*Dicer1*$^{fl/fl}$ animals. (A) Bone marrow cell populations were sorted based on the expression of B220 and IgM from *Cd19*-Cre$^{ki/+}$*Dicer1*$^{fl/+}$ (black bars) and *Cd19*-Cre$^{ki/+}$*Dicer1*$^{fl/fl}$ (white bars) mice and Dicer expression was determined by real-time RT-PCR. Data were normalized to Dicer expression

in B220$^-$ cells from control *Cd19*-Cre$^{ki/+}$*Dicer1*$^{fl/+}$ mice. Statistical bars represent standard deviation (n=4). (B-C) Normal proportions of prepro, pro and pre B cells in *Cd19*-Cre$^{ki/+}$*Dicer1*$^{fl/fl}$ mice. Cell suspensions from bone marrow of *Cd19*-Cre$^{ki/+}$*Dicer1*$^{fl/+}$ and *Cd19*-Cre$^{ki/+}$*Dicer1*$^{fl/fl}$ mice were stained with anti-CD19, anti-B220 and anti-IgM and analysed by flow cytometry. Each point in the graphs represents the percentage of a different B cell subset for an individual animal. (B) Percentage of B220$^+$CD19$^-$ prepro B cells (n=8, p=0.48). (C) Percentage of B220$^+$IgM$^-$ pro and pre B cells (n=6, p=0.68). Filled circles represent *Cd19*-Cre$^{ki/+}$*Dicer1*$^{fl/+}$ control animals, triangles represent *Cd19*-Cre$^{ki/+}$*Dicer1*$^{fl/fl}$ dicer deficient animals. Mean values are represented with horizontal bars. (D) Cell number of B220$^-$ and B220$^+$ populations in spleen. Absolute numbers of B220$^-$ and B220$^+$ cells in *Cd19*-Cre$^{ki/+}$*Dicer1*$^{fl/+}$ and *Cd19*-Cre$^{ki/+}$*Dicer1*$^{fl/fl}$ mice were determined after counting of total spleen cell numbers, anti-B220 staining and flow cytometry analysis. Each point represents B220$^-$ (left) or B220$^+$ (right) absolute number for an individual animal. Filled circles represent *Cd19*-Cre$^{ki/+}$*Dicer1*$^{fl/+}$ control animals, triangles represent *Cd19*-Cre$^{ki/+}$*Dicer1*$^{fl/fl}$ dicer deficient animals (B220$^-$: n=32-34, p=0.16; B220$^+$: n=32-34, p<0.01). Mean values are represented by horizontal bars and shown in Table S1. (E) Dicer expression in non-B cells is not altered in *Cd19*-Cre$^{ki/+}$*Dicer1*$^{fl/fl}$ mice. B220$^-$ cells were sorted from spleen of *Cd19*-Cre$^{ki/+}$*Dicer1*$^{fl/+}$ (black bars) and *Cd19*-Cre$^{ki/+}$*Dicer1*$^{fl/fl}$ (white bars) mice and Dicer expression was determined by real-time RT-PCR. Data were normalized to Dicer expression in B220$^-$ cells from control *Cd19*-Cre$^{ki/+}$*Dicer1*$^{fl/+}$ mice. Statistical bars represent standard deviation (n=3, p=0.23). (F-G) Normal proportions of T cells and macrophages in *Cd19*-Cre$^{ki/+}$*Dicer1*$^{fl/fl}$ mice. Cell suspensions were prepared from spleen of *Cd19*-Cre$^{ki/+}$*Dicer1*$^{fl/+}$ and *Cd19*-Cre$^{ki/+}$*Dicer1*$^{fl/fl}$ mice, stained with anti-CD3 and anti-Mac1 and analysed by flow cytometry. Each point represents an individual animal. (F) Percentage of CD3$^+$ T cells within B220$^-$ population (n=9, p=0.43). (G) Percentage of Mac1$^+$ macrophages within B220$^-$ population (n=9, p=0.72). Filled circles represent *Cd19*-Cre$^{ki/+}$*Dicer1*$^{fl/+}$ control animals, triangles represent *Cd19*-

Cre$^{ki/+}$*Dicer1*$^{fl/fl}$ dicer deficient animals. Mean values are represented by horizontal bars. (H) Normal proportions of T regulatory cells in *Cd19*-Cre$^{ki/+}$*Dicer1*$^{fl/fl}$ mice. Cell suspensions were prepared from lymph nodes (LN) and spleen (SP) from *Cd19*-Cre$^{ki/+}$*Dicer1*$^{fl/+}$ (black bars) and *Cd19*-Cre$^{ki/+}$*Dicer1*$^{fl/fl}$ (white bars) mice, stained with anti-CD3, anti-CD4 and anti-CD25 and analysed by flow cytometry. Bars represent the percentage of T regulatory cells (CD4^{+}CD25^{+}) within CD3^{+} T cell population (LN: n=6, p=0.54; SP: n=4, p=0.64). (I) Dicer expression in T regulatory cells is not altered in *Cd19*-Cre$^{ki/+}$*Dicer1*$^{fl/+}$ mice. T regulatory cells were isolated by immunomagnetic sorting from lymph nodes of *Cd19*-Cre$^{ki/+}$*Dicer1*$^{fl/+}$ (black bars) and *Cd19*-Cre$^{ki/+}$*Dicer1*$^{fl/fl}$ (white bars) mice and Dicer expression was determined by real-time RT-PCR. Data were normalized to Dicer expression in T regulatory cells from control *Cd19*-Cre$^{ki/+}$*Dicer1*$^{fl/+}$ mice. Statistical bars represent standard deviation (n=4, p=0.70). (J-K) Quantification of B1a and B1b B cell subsets in spleen (J) (B1a: n=8, p<0.01; B1b: n=7, p=0.02) and peritoneal wash (K) (B1a: n=6, p=0.46; B1b: n=6, p=0.65) from *Cd19*-Cre$^{ki/+}$*Dicer1*$^{fl/+}$ (black bars) and *Cd19*-Cre$^{ki/+}$*Dicer1*$^{fl/fl}$ (white bars) mice determined by flow cytometry analysis after anti-B220, CD43 and CD5 staining. Statistical bars represent standard deviation.

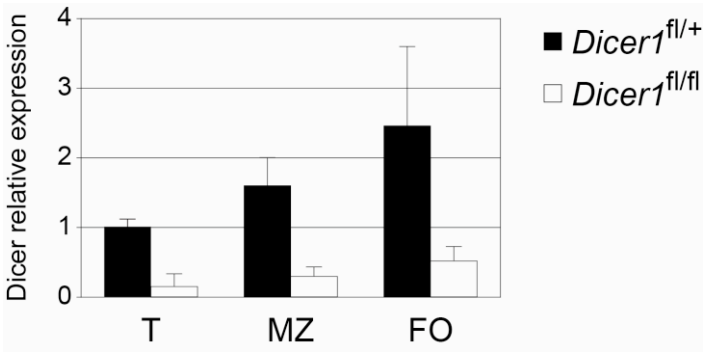

Figure S2, related to Figure 2. Dicer expression in transitional (T), follicular (FO) and marginal zone (MZ) B cell subsets. Spleen B cell populations were sorted based on the expression of B220, CD21, CD23 and CD93 from *Cd19*-Cre$^{ki/+}$*Dicer1*$^{fl/+}$ (black bars) and *Cd19*-Cre$^{ki/+}$*Dicer1*$^{fl/fl}$ (white bars) mice and Dicer expression was determined by real-time RT-PCR. Data were normalized to Dicer expression in transitional (T) cells from control *Cd19*-Cre$^{ki/+}$*Dicer1*$^{fl/+}$ mice. Statistical bars represent standard deviation of three different experiments (T: $p<0.01$; MZ: $p<0.01$; FO: $p=0.04$).

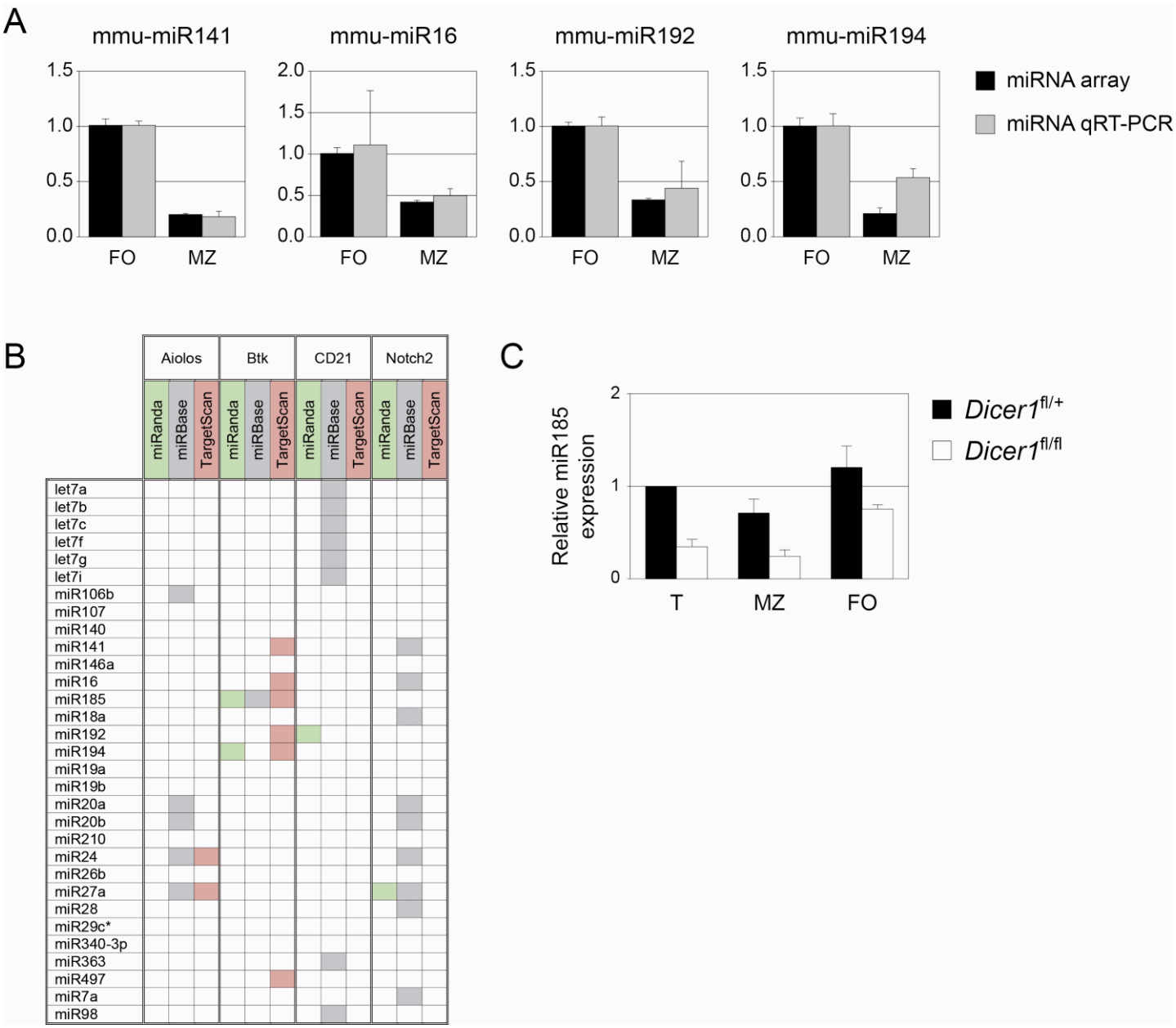

Figure S3, related to Figure 3. MicroRNA expression in B cell subsets. (A) Validation of miRNA microarray results by real-time RT-PCR. Expression of the indicated miRNAs in FO and MZ cells was analysed by real-time RT-PCR (grey bars) and compared to microarray results (black bars) shown in Figure 3a. (B) miR185 is predicted to target Btk mRNA. Aiolos (gene symbol, *Ikzf3*), *Btk*, CD21 (gene symbol, *Cr2*) and *Notch2* genes were subjected to bioinformatic miRNA target prediction analysis using three independent softwares: miRanda (green), miRBase (grey) and TargetScan (red). Predictions for miRNAs found to be

differentially expressed in FO *vs* MZ cells (Fig. 3a) are shown in the table. (C) miR185 expression in transitional (T), follicular (FO) and marginal zone (MZ) B cells. Spleen B cell populations were sorted based on the expression of B220, CD21, CD23 and CD93 from *Cd19*-Cre$^{ki/+}$*Dicer1*$^{fl/+}$ (black bars) and *Cd19*-Cre$^{ki/+}$*Dicer1*$^{fl/fl}$ (white bars) mice and miR185 expression was determined by real-time RT-PCR. Data were normalized to Dicer expression in transitional (T) cells from control *Cd19*-Cre$^{ki/+}$*Dicer1*$^{fl/+}$ mice. Statistical bars represent standard deviation (n=3). (*t* test p values *Cd19*-Cre$^{ki/+}$*Dicer1*$^{fl/+}$ *vs* *Cd19*-Cre$^{ki/+}$*Dicer1*$^{fl/fl}$: T, $p<0.01$; MZ, $p=0.03$; FO, $p=0.03$).

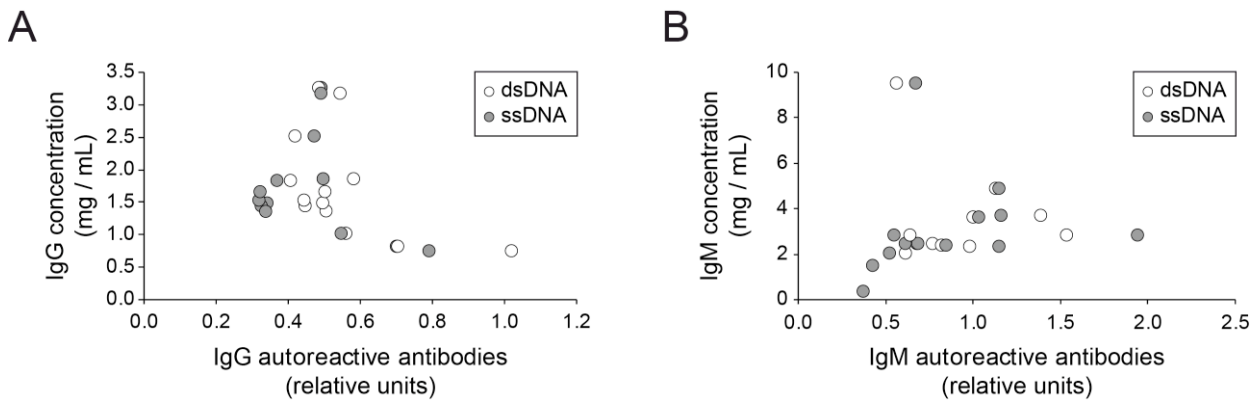

Figure S4, related to Figure 5. There is no correlation between total IgM or IgG titers and autoreactive titers in Dicer deficient females. The plots show total IgG (A) or IgM (B) versus autoreactive IgG (A) or autoreactive IgM (B) anti-ssDNA (closed circles) and anti-dsDNA (opened circles) titers in sera from *Cd19*-Cre$^{ki/+}$*Dicer1*$^{fl/fl}$ aged female mice. Each point in the graphs represents an individual animal (n=12-13).

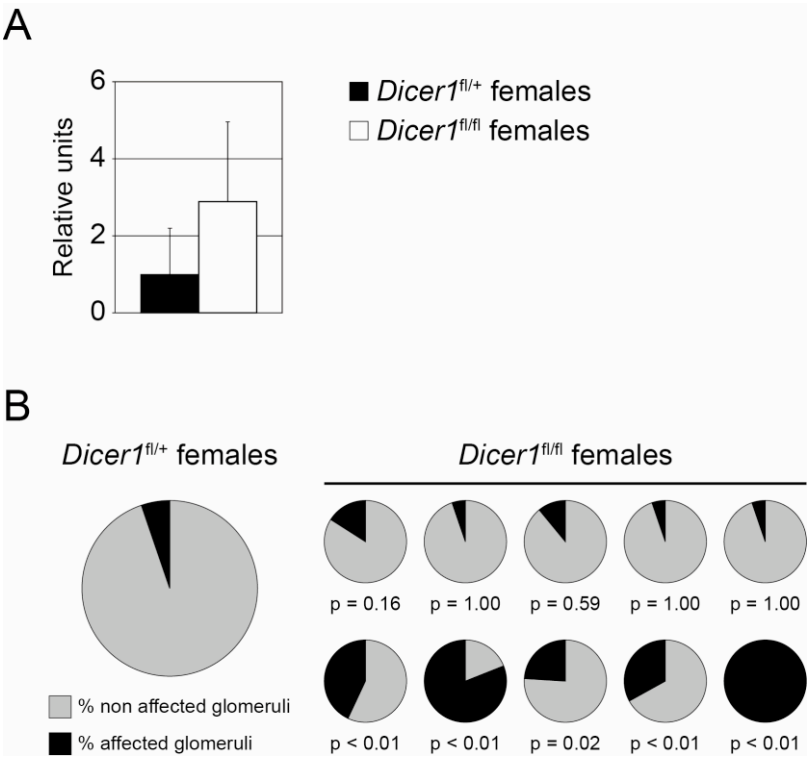

Figure S5, related to Figure 6. Quantification of kidney immunocomplexes and renal damage in *Cd19*-Cre$^{ki/+}$*Dicer1*$^{fl/+}$ and *Cd19*-Cre$^{ki/+}$*Dicer1*$^{fl/fl}$ female mice. (A) Immunofluorecence intensity of kidney stainings from CD19Cre$^{ki/+}$Dicer$^{fl/+}$ and CD19Cre$^{ki/+}$Dicer$^{fl/fl}$ female mice was quantified using LAS AF software. Background was subtracted from mean fluoresce intensity of each glomerulus and obtained values were normalized to control mean ($p<0.01$). (B) The number of damaged glomeruli was determined by kidney sections analysis. Glomerulus damage was established by measuring the periglomerular area using ImageJ software. Graphs represent the percentage of non affected (grey sector) and affected (black sector) glomeruli in a pool CD19Cre$^{ki/+}$Dicer$^{fl/+}$ females and in independent CD19Cre$^{ki/+}$Dicer$^{fl/fl}$ animals. 5 out of 10 dicer deficient females (lower row) showed a significantly increased ($p<0.05$)percentage of damaged glomeruli. P values were calculated using Fisher´s exact test of each CD19Cre$^{ki/+}$Dicer$^{fl/fl}$ mouse against the pool of control animals.

Table S1. Percentage and total cell number of non B cells, B cells and transitional, follicular and marginal zone B cell compartments in spleen of *Cd19*-Cre$^{ki/+}$*Dicer1*$^{fl/+}$ and *Cd19*-Cre$^{ki/+}$*Dicer1*$^{fl/fl}$ mice. [a] Non B cells (B220$^-$), [b] B cells (B220$^+$), [c] Transitional B cells (B220$^+$CD21$^+$CD23^{bright}CD93$^+$), [d] follicular B cells (B220$^+$CD21$^+$CD23^{bright}CD93$^-$), [e] marginal zone B cells (B220$^+$CD21^{bright}CD23$^+$), [f] percentage in total spleen cells, [g] absolute number (x10^6), [h] percentage in total spleen B cells.

			Mean	*SD*	p-value
Non B cells[a]	% [f]	*Dicer1*$^{fl/+}$	48.4	*7.2*	< 0.0001
		Dicer1$^{fl/fl}$	65.0	*7.5*	
	Cell Count [g]	*Dicer1*$^{fl/+}$	35.9	*18.3*	0.1641
		Dicer1$^{fl/fl}$	29.6	*18.1*	
B cells[b]	%[f]	*Dicer1*$^{fl/+}$	51.6	*7.2*	< 0.0001
		Dicer1$^{fl/fl}$	35.0	*7.5*	
	Cell Count [g]	*Dicer1*$^{fl/+}$	39.2	*22.3*	< 0.0001
		Dicer1$^{fl/fl}$	16.0	*11.7*	
T[c]	% [h]	*Dicer1*$^{fl/+}$	16.0	*7.3*	0.0001
		Dicer1$^{fl/fl}$	39.8	*12.8*	
	Cell Count [g]	*Dicer1*$^{fl/+}$	5.8	*3.2*	0.3549
		Dicer1$^{fl/fl}$	7.8	*5.8*	
FO[d]	%[h]	*Dicer1*$^{fl/+}$	60.4	*3.2*	< 0.0001
		Dicer1$^{fl/fl}$	24.1	*8.6*	
	Cell Count [g]	*Dicer1*$^{fl/+}$	21.1	*4.3*	< 0.0001
		Dicer1$^{fl/fl}$	4.5	*3.3*	
MZ[e]	% [h]	*Dicer1*$^{fl/+}$	10.8	*4.8*	0.0009
		Dicer1$^{fl/fl}$	20.8	*6.2*	
	Cell Count [g]	*Dicer1*$^{fl/+}$	3.7	*1.8*	0.8524
		Dicer1$^{fl/fl}$	3.6	*2.0*	

Table S2. Total cell number in transitional, follicular and marginal zone B cell compartments in spleen of 50% *Cd19*-Cre$^{ki/+}$*Dicer1*$^{fl/+}$ and 50% *Cd19*-Cre$^{ki/+}$*Dicer1*$^{fl/fl}$ chimera mice. [a] Transitional B cells (B220$^+$CD21$^+$CD23^{bright}CD93$^+$), [b] follicular B cells (B220$^+$CD21$^+$CD23^{bright}CD93$^-$), [c] marginal zone B cells (B220$^+$CD21^{bright}CD23$^+$), [d] percentage in total spleen B cells, [e] absolute number (x10^6) in total spleen, [f] percentage within CD45.2$^+$ spleen B cells, [g] absolute CD45.2$^+$ number (x10^6).

			T[a]		FO[b]		MZ[c]	
			Mean	*SD*	Mean	*SD*	Mean	*SD*
B220+ gated	% [d]	50% *Dicer1*$^{fl/+}$	10.8	*1.0*	55.8	*3.2*	7.0	*0.7*
		50% *Dicer1*$^{fl/fl}$	13.5	*1.5*	55.6	*2.2*	9.4	*2.4*
		p-value	0.0470		0.9340		0.1679	
	Cell count [e]	50% *Dicer1*$^{fl/+}$	2.0	*0.4*	10.3	*2.8*	1.3	*0.3*
		50% *Dicer1*$^{fl/fl}$	2.4	*0.5*	9.8	*1.2*	1.6	*0.3*
		p-value	0.2778		0.7617		0.2246	
B220$^+$ CD45.2$^+$ gated	% [f]	50% *Dicer1*$^{fl/+}$	6.8	*1.0*	60.6	*3.5*	8.7	*1.5*
		50% *Dicer1*$^{fl/fl}$	21.8	*2.4*	34.9	*2.6*	13.8	*2.7*
		p-value	0.0002		0.0001		0.0319	
	Cell count [g]	50% *Dicer1*$^{fl/+}$	1.6	*0.4*	6.7	*2.1*	0.9	*0.3*
		50% *Dicer1*$^{fl/fl}$	1.8	*0.3*	1.3	*0.1*	0.6	*0.2*
		p-value	0.6256		0.0034		0.1720	

Table S3. IgH sequence analysis of *Cd19*-Cre$^{ki/+}$*Dicer1*$^{fl/+}$ and *Cd19*-Cre$^{ki/+}$*Dicer1*$^{fl/fl}$ mice.

[a] CDR3 sequence, [b] Number of arginines (R) and lysines (K) within the CDR3 sequence.

Cd19-Cre$^{ki/+}$*Dicer1*$^{fl/+}$

Clon	DH	JH	CDR3[a]	R+K[b]
53A1	DSP	3	PSMVPL	0
53A2	DSP	3	SPYQLA	0
53A3	DFL	1	PEYYGSSLLG	0
53A4	DSP	3	EGYGKG	1
53A5	DSP	4	DKGVITTTGGH	1
53A6	DQ52	2	LTGT	0
53A7	DSP	1	HGDGNG	0
53A8	DSP	2	VYDGYYAY	0
53A9	DSP	3	GEKDFYP	1
53A10	DQ52	1	PYLGR	1
52A1	DSP	4	SYDYDDGS	0
52A2	DST	2	GTRG	1
52A3	DFL	4	QREITYYGSSYED	1
52A4	DST	3	SG	0
52A5	DST	4	TETAQATR	1
52A6	DFL	2	SYYGSSY	0
52A7	DFL	2	DTTVV	0
52A8	DSP	4	RG	1
52A9	DQ52	1	SGGPL	0
52A10	DSP	3	HDYD	0
50A1	DQ52	3	DSRDGTR	2
50A2	DSP	2	SGRYDL	1
50A3	DSP	4	TYYSKG	1
50A4	DFL	2	EGLRLLI	1
50A5	DFL	1	YYYGSSYVG	0
50A6	DFL	2	GYGSSY	0
50A7	DFL	2	DYYGSF	0
50A8	DST	2	EGTPN	0
50A9	DFL	1	PYGSSYD	0
50A10	DFL	4	HEGG	0
48A1	DFL	2	LTTVVA	0
48A2	DQ52	1	HPELGRG	1
48A3	DSP	4	IEGNYN	0
48A4	DSP	3	EGVYDYDG	0
48A5	DFL	2	GVYYYG	0
48A6	DFL	3	SLLLRHGFKG	2
53B1	DST	2	SERG	1
53B2	DST	3	KDSSGYVG	1
53B3	DQ52	2	VGLTL	0
53B4	DSP	4	RGDYYRYDDG	2
53B5	DSP	4	SYYGNYF	0
53B6	DST	3	EGGSSGS	0
53B7	DFL	2	MTTAT	0
53B8	DFL	2	RSYYGYD	1
53B9	DSP	2	SRDYG	1
53B10	DSP	2	SWDGFY	0
52B1	DSP	2	TYSNYGG	0
52B2	DFL	2	SVHYYGV	0
52B3	DSP	2	RDSNYGF	1
52B4	DST	2	SGTV	0
52B5	DST	2	GGSSGYGGY	0
52B6	DSP	3	RSEGNYVS	1
52B7	DSP	1	RIYYGN	1
52B8	DSP	2	DGNP	0
52B9	DSP	3	EGGGNS	0
48B1	DSP	2	ASKNYSPL	1
48B2	DFL	2	LNYGH	0
48B3	DSP	2	LEMVKN	1
48B4	DFL	1	ARWYYGSPS	1
48B5	DQ52	2	SSGT	0
48B6	DFL	3	STTVVEPS	0
48B7	DSP	4	SYGNS	0
48B8	DFL	1	YYGSS	0
48B9	DFL	2	YYYGSSL	0
48B10	DSP	2	RDGMY	1
50B2	DSP	4	GGIYYDYD	0
50B3	DSP	1	AVTTSR	1
50B4	DFL	3	TGSSS	0
50B5	DFL	3	GGSITTASG	0
50B6	DSP	4	PIYP	0
50B7	DQ52	4	LGAGTGS	0
50B8	DFL	1	LYYGSL	0
50B9	DSP	2	GDYRYDVS	1
50B10	DSP	2	KGG	1

Cd19-Cre$^{ki/+}$*Dicer1*$^{fl/fl}$

Clon	DH	JH	CDR3[a]	R+K[b]
55A1	DQ52	3	GQLTGT	0
55A2	DSP	3	SPYDGY	0
55A3	DSP	3	RDYD	1
55A4	DSP	1	SRIYYDYDA	1
55A5	DSP	4	PYDYH	0
55A6	DFL	1	QAHYYGSRGG	1
55A7	DSP	2	GRGWGN	1
55A8	DSP	4	RSTMITTL	1
55A9	DFL	2	SIYYYGSRA	1
55A10	DQ52	3	SNWDG	0
56A1	DSP	2	HAGTGGD	0
56A2	DSP	3	QGLRG	1
56A3	DQ52	4	LGRE	1
56A4	DFL	2	HRTPGSSF	1
56A5	DSP	3	SFYDY	0
56A6	DSP	4	SGNYVT	0
56A7	DST	4	GVPH	0
56A8	DFL	2	HTV	0
56A9	DSP	1	QGG	0
56A10	DFL	4	TFYYGP	0
54A1	DSP	2	HGN	0
54A2	DSP	3	GYRYDE	1
54A3	DSP	2	GYGN	0
54A4	DFL	1	HYYGSS	0
54A5	DSP	2	RGGNYED	1
54A6	DSP	2	DGN	0
54A7	DSP	3	SRIYYGP	1
54A8	DFL	3	GLGVRL	1
54A9	DSP	4	QGGLRRVS	2
54A10	DFL	4	RYVE	1
51A1	DSP	4	HGDYDG	0
51A2	DQ52	3	TN	0
51A3	DSP	4	LMGTYGYDGED	0
51A4	DSP	4	DYRG	1
51A5	DSP	1	RYGYDD	1
54B1	DQ52	2	RLGP	1
54B2	DQ52	2	GGD	0
54B3	DSP	4	SYYDYD	0
54B4	DQ52	2	RGT	1
54B5	DSP	2	SVRRY	2
54B6	DSP	3	GDYDYDGP	0
54B7	DSP	4	TNYYR	1
54B8	DSP	3	YGNYE	0
54B9	DSP	2	RTM	1
54B10	DST	4	RQLGLP	1
55B1	DFL	3	DDYYGSRS	1
55B2	DFL	2	RTG	1
55B3	DST	2	SGSSGYVG	0
55B4	DFL	4	RGS	1
55B5	DST	4	GELSRPRQLGLQD	2
55B6	DSP	2	GGVTTVVP	0
55B7	DSP	2	ARLGLF	1
55B8	DSP	4	VTRYGYDPR	2
55B9	DFL	4	SGFYYGYD	0
55B10	DFL	3	LTTATTP	0
56B1	DFL	4	GGSSYR	1
56B2	DSP	3	TIPGG	0
56B3	DFL	4	SNYYGSS	0
56B4	DSP	2	WYYRY	1
56B5	DFL	4	REVVATY	1
56B6	DSP	2	EGWLLH	0
56B7	DSP	4	HRGYED	1
56B8	DFL	3	KTLRLQ	2
56B9	DFL	4	TVLLD	0
56B10	DFL	4	WDYYGSSLH	0
51B1	DSP	1	KGTGYV	1
51B2	DSP	4	QG	0
51B3	DSP	4	GGVRG	1
51B4	DSP	3	SLYGTHEG	0
51B5	DST	2	GTGR	1
51B6	DFL	3	RLRGR	3
51B7	DSP	1	SFYDGYPRG	1
51B8	DSP	2	SMIT	0
51B9	DFL	2	VHYYGYS	0
51B10	DSP	2	WGMIRN	1

nature immunology

Ribose 2′-*O*-methylation provides a molecular signature for the distinction of self and non-self mRNA dependent on the RNA sensor Mda5

Roland Züst[1,10,11], Luisa Cervantes-Barragan[1,11], Matthias Habjan[1], Reinhard Maier[1], Benjamin W Neuman[2], John Ziebuhr[3,4], Kristy J Szretter[5], Susan C Baker[6], Winfried Barchet[7], Michael S Diamond[5], Stuart G Siddell[8], Burkhard Ludewig[1,9] & Volker Thiel[1,9]

The 5′ cap structures of higher eukaryote mRNAs have ribose 2′-*O*-methylation. Likewise, many viruses that replicate in the cytoplasm of eukaryotes have evolved 2′-*O*-methyltransferases to autonomously modify their mRNAs. However, a defined biological role for 2′-*O*-methylation of mRNA remains elusive. Here we show that 2′-*O*-methylation of viral mRNA was critically involved in subverting the induction of type I interferon. We demonstrate that human and mouse coronavirus mutants lacking 2′-*O*-methyltransferase activity induced higher expression of type I interferon and were highly sensitive to type I interferon. Notably, the induction of type I interferon by viruses deficient in 2′-*O*-methyltransferase was dependent on the cytoplasmic RNA sensor Mda5. This link between Mda5-mediated sensing of viral RNA and 2′-*O*-methylation of mRNA suggests that RNA modifications such as 2′-*O*-methylation provide a molecular signature for the discrimination of self and non-self mRNA.

Innate immune recognition of pathogen-associated molecular patterns facilitates the distinction between immunological self and non-self[1]. For cytoplasmic viral RNA, this involves detection by cytoplasmic RIG-I-like receptors, such as RIG-I and Mda5, and the initiation of signaling cascades that induce the expression of cytokines, including type I interferon. Interferon-α (IFN-α) and IFN-β are secreted and signal through the type I interferon receptor (IFNAR) to transmit a danger signal to neighboring cells. The activated IFNAR triggers a signaling pathway consisting of the kinase Jak and STAT transcription factors, inducing the expression of a large array of interferon-stimulated genes encoding molecules with antiviral activity, thus establishing the so-called 'host cell antiviral state'[2–4]. These interferon-stimulated genes include those encoding the protein kinase PKR, as well as stress-inducible proteins such as IFIT1 and IFIT2 (also known as ISG56 and ISG54, respectively), which impair the host cell protein synthesis apparatus[4–7].

Although the distinction between self and non-self RNA is believed to rely on the molecular signatures found in pathogen-associated molecular patterns, the exact nature of such signatures remains elusive. Both cytosolic RIG-I-like receptors (RIG-I and Mda5) bind to double-stranded RNA (dsRNA); however, RIG-I seems to 'prefer' short dsRNA, whereas Mda5 can specifically bind long dsRNA[8]. In addition, RIG-I can specifically recognize 5′-triphosphate groups on single-stranded RNA and (partially) dsRNA[9–11]. In contrast, eukaryotic mRNA, which is not recognized by RIG-I or Mda5, usually has a 5′ cap structure methylated at the N7 position of the capping guanosine residue (cap 0), the ribose-2′-*O* position of the 5′-penultimate residue (cap 1) and sometimes at adjoining residues (cap 2)[12]. Two evolutionary forces are thought to be responsible for the presence of 5′ cap structures on eukaryotic mRNA: the appearance of 5′ exonucleases in eukaryotes and the need for a means of directing mRNA to the eukaryotic ribosome[13]. Thus, eukaryotic mRNA 5′ cap structures are known to increase mRNA stability and translational efficacy. Notably, although N7 methylation is important in many mRNA-related processes, such as transcriptional elongation, polyadenylation, splicing, nuclear export and efficient translation, there is no obvious reason for the evolution of 2′-*O*-methylation of mRNA ribose in cap 1 and cap 2 structures in higher eukaryotes.

The functional importance of mRNA 5′-structures is inferred from the fact that many viruses that replicate in the cytoplasm (such as picornaviruses, flaviviruses, coronaviruses and poxviruses) have evolved alternative 5′ elements, such as small viral proteins linked to the 5′ end of genomic RNA[14], or encode functions associated with the formation of a 5′ cap that are homologous to those found in eukaryotic

[1]Institute of Immunobiology, Kantonal Hospital St. Gallen, St. Gallen, Switzerland. [2]School of Biological Sciences, University of Reading, Reading, UK. [3]Centre for Infection and Immunity, Queen's University Belfast, Belfast, UK. [4]Institute of Medical Virology, Justus Liebig University Giessen, Giessen, Germany. [5]Department of Medicine, Department of Molecular Microbiology, and Department of Pathology & Immunology, Washington University School of Medicine, St. Louis, Missouri, USA. [6]Department of Microbiology and Immunology, Loyola University Stritch School of Medicine, Maywood, Illinois, USA. [7]Institute for Clinical Chemistry and Pharmacology, University Hospital, University of Bonn, Bonn, Germany. [8]Department of Cellular and Molecular Medicine, School of Medical and Veterinary Sciences, University of Bristol, Bristol, UK. [9]Vetsuisse Faculty, University of Zürich, Zürich, Switzerland. [10]Present address: Singapore Immunology Network, Agency for Science, Technology and Research, Singapore. [11]These authors contributed equally to this work. Correspondence should be addressed to V.T. (volker.thiel@kssg.ch).

Received 2 November 2010; accepted 2 December 2010; published online 9 January 2011; doi:10.1038/ni.1979

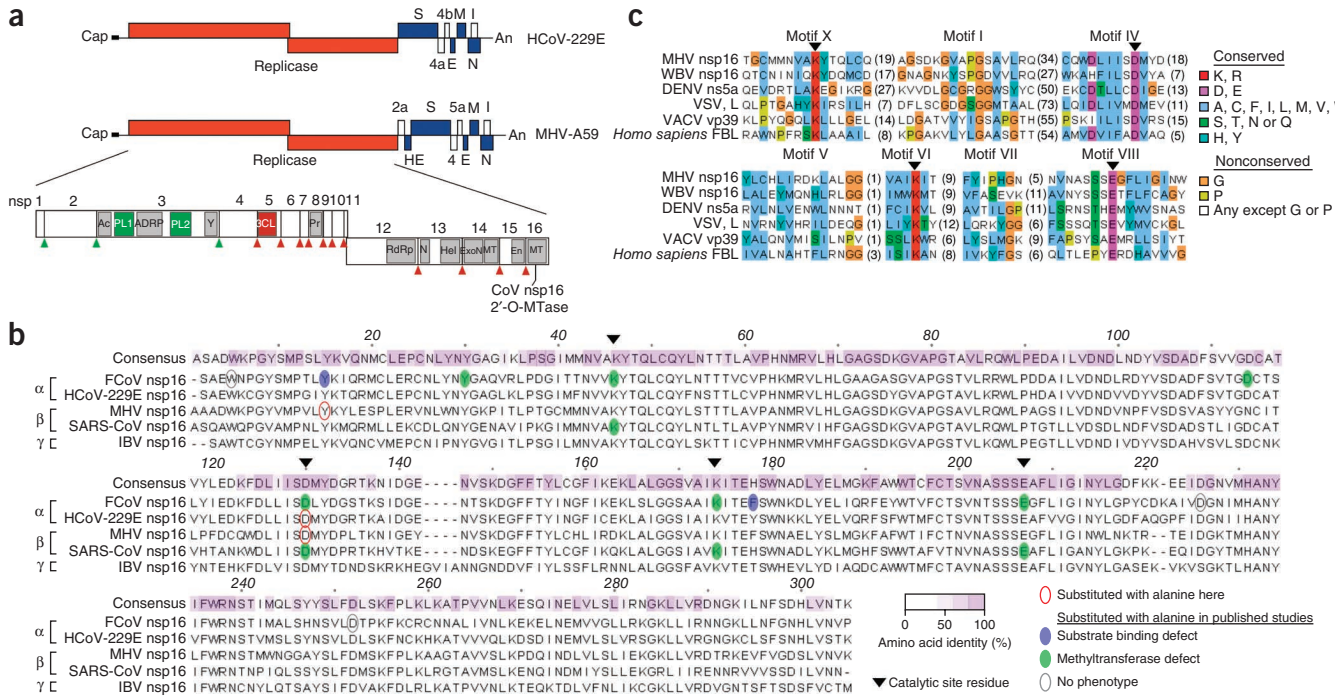

Figure 1 Conservation of viral 2′-*O*-methyltransferases. (**a**) Human and mouse coronavirus genomes, including viral open reading frames (boxes; labels above and below identify gene products). The replicase gene, including conserved domains and viral proteinase cleavage sites (upward arrowheads) that separate nsp1–nsp16, is enlarged. CoV nsp16 MTase, nsp16-associated 2′-*O*-methyltransferase. (**b**) ClustalW2 alignment of coronavirus nsp16 amino acid sequences, representative of α-, β- and γ-coronaviruses. Keys (bottom right) identify sequence conservation (amino acid identity), amino acid substitutions and phenotypes of mutant proteins. FCoV, feline coronavirus; MHV, MHV strain A59; SARS-CoV, severe acute respiratory syndrome coronavirus; IBV, infectious bronchitis virus. (**c**) Comparison of the sequences of viral and cellular methyltransferase motifs. WBV, white bream virus (order Nidovirales); DENV, dengue virus (family Flaviviridae); VSV, vesicular stomatitis virus (order Mononegavirales); VACV, vaccinia virus (family Poxviridae); FBL, fibrillarin (*Homo sapiens*). Right, key for amino acid similarity (single-letter codes) and conservation according to default ClustalX.

cells, such as RNA 5′-triphosphatase, RNA guanylyltransferase, RNA guanine-N7-methyltransferase (N7-methyltransferase), and 2′-*O*-methyltransferase. The fact that RNA 5′-triphosphate groups activate RIG-I (refs. 9,10) suggests that viruses must hide or modify their RNA 5′ structures to evade innate immune recognition. In addition, RIG-I activation is diminished when 5′-triphosphate RNA contains modified nucleotides[9]. Thus, RNA modifications such as methylation could be critical factors for the activation of RNA-specific pattern-recognition receptors. Notably, this idea of methylation-based distinction of self and non-self nucleic acids is well established for DNA, as the methylation status of CpG dinucleotide motifs in DNA is the structural basis of the activation of Toll-like receptor 9 (TLR9)[15]. Moreover, DNA methylation represents the basis for the ancient bacterial restriction and modification systems that allow bacteria to distinguish between foreign DNA and the bacterial genome.

Here we show that 2′-*O*-methylation of viral mRNA is biologically important in the context of innate immune responses in the host cell. We demonstrate that human and mouse coronavirus mutants lacking 2′-*O*-methyltransferase activity induced higher expression of type I interferon and were extremely sensitive to type I interferon treatment. Furthermore, a mouse coronavirus mutant with an inactivated 2′-*O*-methyltransferase was attenuated in wild-type macrophages but replicated efficiently in the absence of IFNAR or Mda5. The coronavirus 2′-*O*-methyltransferase mutants were apathogenic in wild-type mice; however, viral replication and spreading was restored in mice lacking IFNAR and in mice lacking TLR7 and Mda5, the two main sensors of coronavirus RNA. Collectively our results show a link between Mda5-mediated sensing of viral RNA and 2′-O-methylation of mRNA and suggest that RNA modifications such as 2′-O-methylation provide a molecular signature for the distinction of self and non-self mRNA.

RESULTS

Deficiency in 2′-*O*-methyltransferase in human coronavirus infection

Coronaviruses are single-stranded (+) RNA viruses that replicate in the cytoplasm and have evolved N7-methyltransferases and 2′-*O*-methyltransferases to methylate their viral mRNA 5′ cap structures[16–19]. The coronavirus 2′-*O*-methyltransferase activity is associated with the viral nonstructural protein nsp16, which is highly conserved among coronaviruses (**Fig. 1a**,**b**), and an integral subunit of the viral replicase-transcriptase complexes located at virus-induced double-membraned vesicles in the host cell cytoplasm. Coronavirus 2′-*O*-methyltransferase belongs to the human fibrillarin and *Escherichia coli* RrmJ-like methyltransferase family[20] that includes many viral and cellular homologs (**Fig. 1c** and **Supplementary Table 1**).

To address the biological importance of 2′-*O*-methylation of mRNA in the context of host cell innate immune responses, we first used a human model of coronavirus infection. We generated a mutant of the recombinant human coronavirus strain 229E (HCoV-229E) with an inactivated 2′-*O*-methyltransferase. We produced this mutant by substituting alanine for the aspartic acid at position 129 of the highly conserved catalytic KDKE tetrad of nsp16 (HCoV-D129A; **Fig. 1b**). Notably, this substitution completely abrogates the 2′-*O*-methyltransferase activity of recombinant, bacteria-expressed nsp16 proteins of feline coronavirus and severe acute respiratory syndrome coronavirus[16,18]. The mutant virus had a small plaque phenotype and less replication in the human fibroblast MRC-5 cell line (**Fig. 2a**,**b**).

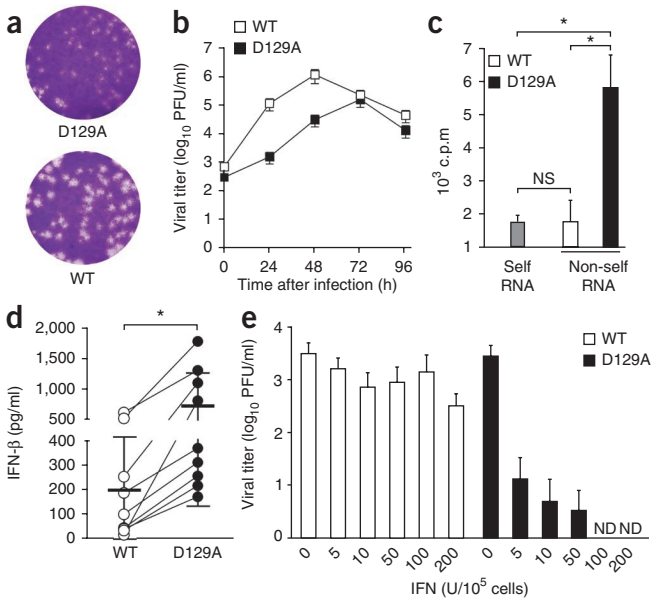

Figure 2 The HCoV 2′-*O*-methyltransferase mutant has altered replication kinetics and induction of and sensitivity to type I interferon. (**a**) Plaque assay of HCoV-229E and HCoV-D129A. (**b**) Replication kinetics of wild-type HCoV-229E (WT) and the mutant HCoV-D129A (D129A) in MRC-5 cells infected at an MOI of 0.1, presented as viral titer in plaque-forming units (PFU). (**c**) Incorporation of ^{3}H into poly(A)-containing RNA derived from mock-infected cells (Self RNA) or cells infected with HCoV-229E or HCoV-D129A (Non-self RNA) after *in vitro* 2′-*O*-methylation with VP39. NS, not significant ($P > 0.05$); $^{*}P < 0.01$ (unpaired Student's *t*-test). (**d**) Enzyme-linked immunosorbent assay of IFN-β in supernatants of human blood–derived macrophages 24 h after infection with HCoV-229E or HCoV-D129A (MOI = 1). Each symbol represents an individual donor ($n = 9$); thick horizontal lines indicate the mean (thin horizontal lines, s.d.). $^{*}P < 0.005$ (Wilcoxon matched-pairs test). (**e**) Plaque assay of viral titers in human blood–derived macrophages pretreated with increasing doses of IFN-α (horizontal axis) 4 h before infection with HCoV-229E or HCoV-D129A (MOI = 1), assessed 24 h after infection. ND, not detected. Data are representative of three experiments (**a**) or represent two (**b**,**e**) or three (**c**,**d**) independent experiments (average and s.e.m. of triplicates in **b**; mean and s.d. in **c**; error bars, s.d. of six samples in **e**).

We were able to readily methylate poly(A)-containing RNA from HCoV-D129A-infected cells using the vaccinia virus 2′-*O*-methyltransferase VP39 *in vitro*[21] (**Fig. 2c**), which confirmed the loss of 2′-*O*-methyltransferase activity by HCoV-D129A. In contrast, *in vitro* 2′-*O*-methylation of poly(A)-containing RNA derived from HCoV-229E-infected cells was indistinguishable from the 2′-*O*-methylation of poly(A)-containing RNA obtained from mock-infected cells. We observed significantly higher IFN-β expression in blood-derived human macrophages after infection with HCoV-D129A than after infection with HCoV-229E, (**Fig. 2d**) and complete restriction of HCoV-D129A replication in human macrophages pretreated with IFN-α (**Fig. 2e**). These results suggest a biological role for 2′-*O*-methylation of mRNA in the context of the induction of type I interferon and antiviral effector mechanisms stimulated by type I interferon.

Mda5-dependent induction of type I interferon

To extend our studies on the effect of 2′-*O*-methylation on coronavirus-induced innate immune responses, we used an animal model of coronavirus infection with mouse hepatitis virus strain A59 (MHV-A59) as a natural mouse pathogen. Plasmacytoid dendritic cells have a unique and crucial role in sensing coronavirus RNA via TLR7 that ensures the swift production of type I interferon after viral encounter[22,23]. Other target cells such as primary fibroblasts, neurons, astrocytes, hepatocytes and conventional dendritic cells do not have detectable production of type I interferon after infection with MHV[23,24]. The exceptions to that are macrophages and microglia, which can respond with expression of type I interferon after MHV infection, although only to moderate amounts[25,26]. The expression of type I interferon detected in macrophages and microglia is dependent on Mda5 (ref. 25).

We generated a recombinant MHV lacking 2′-*O*-methyltransferase activity by substituting alanine for the aspartic acid at the 2′-*O*-methyltransferase active site at position 130 of nsp16 (MHV-D130A;

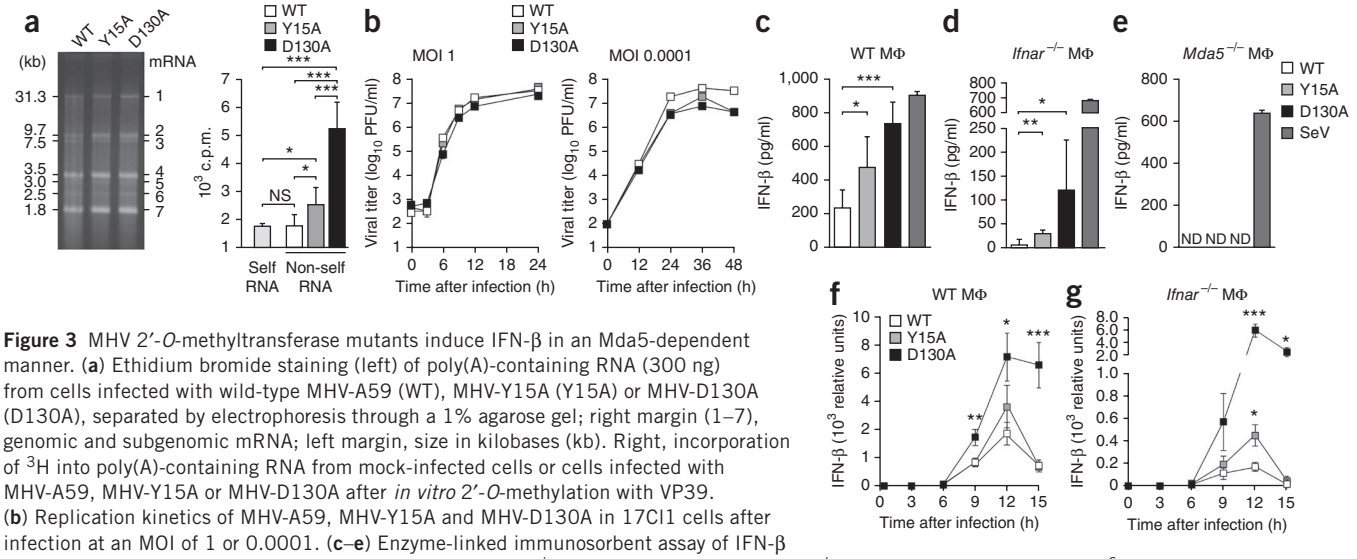

Figure 3 MHV 2′-*O*-methyltransferase mutants induce IFN-β in an Mda5-dependent manner. (**a**) Ethidium bromide staining (left) of poly(A)-containing RNA (300 ng) from cells infected with wild-type MHV-A59 (WT), MHV-Y15A (Y15A) or MHV-D130A (D130A), separated by electrophoresis through a 1% agarose gel; right margin (1–7), genomic and subgenomic mRNA; left margin, size in kilobases (kb). Right, incorporation of ^{3}H into poly(A)-containing RNA from mock-infected cells or cells infected with MHV-A59, MHV-Y15A or MHV-D130A after *in vitro* 2′-*O*-methylation with VP39. (**b**) Replication kinetics of MHV-A59, MHV-Y15A and MHV-D130A in 17Cl1 cells after infection at an MOI of 1 or 0.0001. (**c**–**e**) Enzyme-linked immunosorbent assay of IFN-β in supernatants of wild-type (WT; **c**), IFNAR-deficient (*Ifnar*$^{-/-}$; **d**) or Mda5-deficient (*Mda5*$^{-/-}$; **e**) macrophages (MΦ; 1×10^{6}) infected with wild-type or mutant MHV or Sendai virus (SeV) at an MOI of 1 and assessed 15 h after infection. (**f**,**g**) Quantitative RT-PCR analysis of the kinetics of IFN-β mRNA expression in wild-type (**f**) or IFNAR-deficient (**g**) macrophages (1×10^{6}) infected with MHV-A59, MHV-Y15A or MHV-D130A (MOI = 1), presented relative to its expression in uninfected cells. $^{*}P < 0.05$, $^{**}P < 0.01$ and $^{***}P < 0.001$ (unpaired Student's *t*-test). Data represent seven (**a**), two (**b**,**f**,**g**) or three (**c**–**e**) independent experiments (mean and s.d. of seven (**a**) or six (**c**–**g**) samples, or mean and s.e.m. of six samples (**b**)).

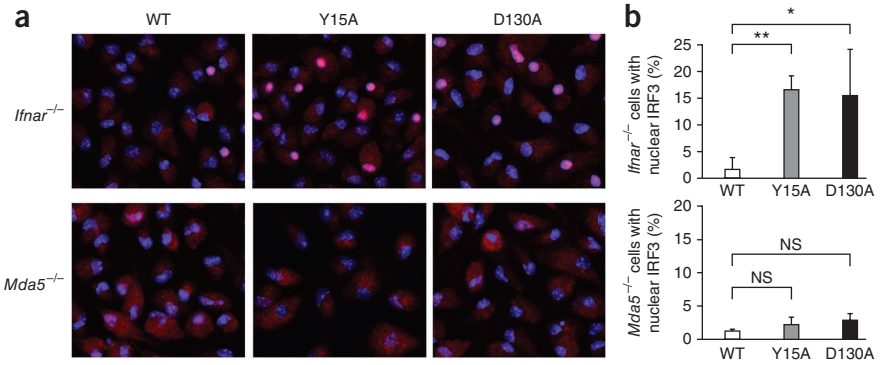

Figure 4 MHV 2′-*O*-methyltransferase mutants induce the nuclear localization of IRF3 in an Mda5-dependent manner. (**a**) IRF3 in IFNAR-deficient or Mda5-deficient mouse macrophages infected with MHV-A59, MHV-Y15A or MHV-D130A at an MOI of 1 and stained at 3 h after infection for IRF3 (red) and with the DNA-intercalating dye DAPI (blue). Original magnification, ×20. Data are representative of three experiments. (**b**) Frequency of cells (infected as in **a**) with nuclear IRF3. $*P < 0.01$ and $**P < 0.001$ (unpaired Student's *t*-test). Data are representative of three experiments (mean and s.d. of five random fields with approximately 50–250 cells each).

Fig. 1b). In addition, we generated a recombinant MHV mutant with a tyrosine-to-alanine substitution at the putative cap 0–binding site of nsp16 (MHV-Y15A; **Fig. 1b**). This substitution impairs cap 0 binding for the corresponding feline coronavirus nsp16 mutant Y14A[18], and we expected that this substitution would result in less 2′-*O*-methylation of coronaviral mRNA, rather than complete abrogation of this. Indeed, *in vitro* methylation of mRNA with the vaccinia virus 2′-*O*-methyltransferase VP39 (ref. 21) confirmed the differences in 2′-*O*-methylation of mRNA obtained from MHV-infected cells. The transfer of ^{3}H-labeled methyl groups from the methyl donor *S*-adenosyl-methionine to mRNA was less efficient for mRNA derived from MHV-Y15A-infected cells than for mRNA from MHV-D130A-infected cells but significantly more efficient than for mRNA from MHV-A59-infected cells (**Fig. 3a**). These results demonstrate the loss of 2′-*O*-methyltransferase activity by MHV-D130A and show that a considerable proportion of MHV-Y15A mRNA is not methylated at the 2′-*O* position.

In cell culture, the replication kinetics of the mutant viruses MHV-D130A and MHV-Y15A differed only slightly from those of MHV-A59 after infection of the mouse fibroblast cell line 17Cl1 at a high multiplicity of infection (MOI) or low MOI (1 or 0.0001, respectively; **Fig. 3b**). Also, there was no notable difference among cells infected with MHV-A59, MHV-D130A or MHV-Y15A in the formation and morphology of double-membraned vesicles in the cytoplasm, as observed by electron microscopy (**Supplementary Fig. 1**). That observation is relevant to the cytoplasmic sensing of viral RNA, as coronavirus double-membraned vesicles are known to contain dsRNA. Infection with either of the 2′-*O*-methyltransferase mutants (MHV-Y15A or MHV-D130A) resulted in more production of type I interferon in wild-type macrophages at 15 h after infection (**Fig. 3c** and **Supplementary Fig. 2a**). Likewise, type I interferon was efficiently produced in IFNAR-deficient macrophages infected with MHV-D130A or MHV-Y15A (**Fig. 3d** and **Supplementary Fig. 2b**), which indicated that the MHV 2′-*O*-methyltransferase mutants triggered the production of type I interferon in the absence of IFNAR signaling. Neither MHV-A59 nor the two 2′-*O*-methyltransferase mutant viruses induced any detectable expression of type I interferon in Mda5-deficient macrophages (**Fig. 3e**), whereas the production of type I interferon was readily detectable in Mda5-deficient cells after infection with Sendai virus. Detailed analysis of the kinetics of IFN-β mRNA expression showed that infection of wild-type macrophages (**Fig. 3f**) and IFNAR-deficient macrophages (**Fig. 3g**) with MHV-D130A or MHV-Y15A resulted in higher expression of the gene encoding IFN-β (with a peak at 12 h after infection) than did MHV-A59 infection. Notably, the induction of IFN-β was greatest after infection with MHV-D130A, which has a mutant 2′-*O*-methyltransferase active site. These results indicate that deficiency in 2′-*O*-methylation in viral RNA induces higher IFN-β expression and that IFN-β induction after infection with viruses with mutant 2′-*O*-methyltransferases is Mda5 dependent.

Interferon-regulatory factor 3 (IRF3) is activated by RIG-I-like receptor signaling and translocates to the nucleus to mediate the transcription of genes encoding type I interferons. We observed more nuclear localization of IRF3 in IFNAR-deficient macrophages infected with MHV-D130A or MHV-Y15A but not in Mda5-deficient macrophages (**Fig. 4**). Collectively these results demonstrate that

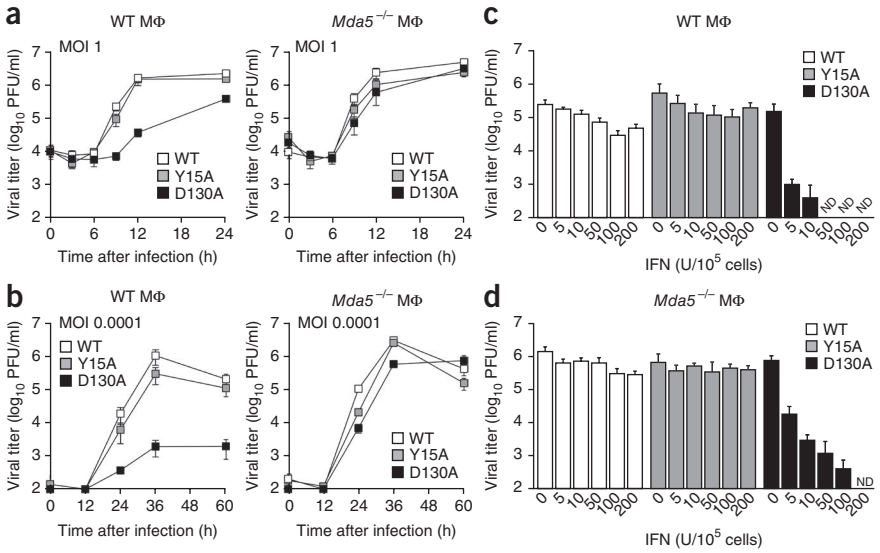

Figure 5 Differences in the effect of type I interferon on the replication of MHV 2′-*O*-methyltransferase mutants. (**a**,**b**) Kinetics of the replication of MHV-A59, MHV-Y15A or MHV-D130A in wild-type and Mda5-deficient mouse macrophages (1×10^6) after infection at an MOI of 1 (**a**) or 0.0001 (**b**). Data represent two independent experiments (mean ± s.e.m. of five samples). (**c**,**d**) Titer of MHV-A59, MHV-Y15A or MHV-D130A at 24 h after infection (MOI = 1) of wild-type (**c**) or Mda5-deficient (**d**) macrophages (1×10^5) pretreated with IFN-α (dose, horizontal axis) 4 h before infection. Data represent two independent experiments (mean and s.d. of four samples).

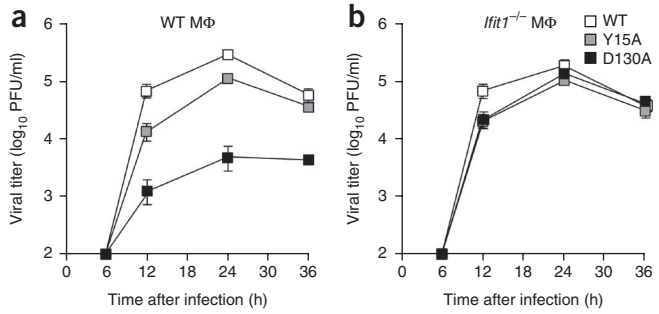

Figure 6 Restoration of MHV-D130A replication in IFIT1-deficient macrophages. Kinetics of the replication of MHV-A59, MHV-Y15A or MHV-D130A after infection (MOI = 0.01) of wild-type mice (**a**) or IFIT1-deficient (**b**) macrophages (5×10^5), assessed by plaque assay of viral titers in supernatants. Data represent two independent experiments (mean ± s.e.m. of four samples).

2′-*O*-methylation of mRNA is linked to the induction of IFN-β expression in an Mda5-dependent manner.

Two distinct antiviral mechanisms affected by 2′-*O*-methylation

As HCoV-D129A, the human coronavirus with a mutant 2′-*O*-methyltransferase active site, showed greater sensitivity to treatment with type I interferon, we assessed whether type I interferon–induced restriction of viral replication was also effective against the MHV 2′-*O*-methyltransferase mutants. We investigated the viral replication kinetics of MHV-D130A and MHV-Y15A in primary macrophages, which represent the most important target cells for MHV[22,27]. MHV-D130A replication was considerably impaired in wild-type macrophages (even after infection at a high MOI of 1), whereas the replication of MHV-Y15A was similar to that of MHV-A59 (**Fig. 5a**). MHV-D130A replication was fully restored in Mda5-deficient macrophages, even after infection at a low MOI of 0.0001 (**Fig. 5b**). This demonstrates that Mda5-dependent expression of type I interferon is a prerequisite for the induction of effective restriction of MHV-D130A replication. In agreement with the idea that MHV-D130A replication was impaired in wild-type macrophages, but MHV-Y15A replication was not, we observed much less replication of MHV-D130A in macrophages pretreated with IFN-α. Thus, in contrast to MHV-A59, MHV-D130A was not detectable at 24 h after infection after 4 h of pretreatment of wild-type macrophages with 50–200 units of IFN-α, whereas MHV-Y15A replication was not restricted much (**Fig. 5c**). In Mda5-deficient macrophages, pretreatment with at least 200 units of IFN-α was needed to restrict MHV-D130A replication to undetectable amounts (**Fig. 5d**), which suggested that endogenous expression of type I interferon mediated by Mda5 affected the MHV-D130A restriction in wild-type macrophages. These data indicate that the D130A and Y15A substitutions of MHV nsp16 had different effects on the induction of type I interferon and viral replication. The D130A substitution led to more production of type I interferon as well as to considerable sensitivity to pretreatment with type I interferon. In contrast, the Y15A substitution induced more production of type I interferon but not more sensitivity to type I interferon. Thus, we conclude that in addition to triggering Mda5-dependent induction of type I interferon, loss of 2′-*O*-methylation triggers a second antiviral mechanism that is induced by type I interferon and accounts for the restriction of viral replication during the host cell antiviral state.

The replication of a mutant of West Nile virus (family Flaviviridae; genus *Flavivirus*) lacking 2′-*O*-methylation is considerably inhibited by members of the IFIT family[28], which are encoded by interferon-stimulated genes linked to translational regulation. To assess whether this molecular mechanism is also relevant to coronavirus infection, we analyzed the replication kinetics of MHV-A59, MHV-D130A and MHV-Y15A in primary macrophages derived from wild-type or IFIT1-deficient mice. MHV-D130A replication was almost completely restored in IFIT1-deficient macrophages (**Fig. 6**), analogous to the restoration of MHV-D130A replication in Mda5-deficient macrophages (**Fig. 5a**,**b**). These results suggest that the Mda5-dependent induction of type I interferon and the IFIT-1-mediated restriction of viral replication are two distinct antiviral mechanisms based on the distinction between 2′-*O*-methylated mRNA and nonmethylated mRNA.

Effect of 2′-*O*-methylation on innate immune recognition *in vivo*

Next we examined the effect of 2′-*O*-methylation of viral mRNA on innate immune recognition and virulence *in vivo*. We compared the phenotype of MHV-A59 with that of each MHV 2′-*O*-methyltransferase mutant in C57BL/6 mice after intraperitoneal infection with 500 plaque-forming units of virus (**Fig. 7**). In contrast to MHV-A59, neither of the MHV 2′-*O*-methyltransferase mutants was detectable in spleen or liver of C57BL/6 mice at 48 h after infection, which demonstrated the importance of 2′-*O*-methylation of viral mRNA for efficient replication and spread in the host. However, the two MHV 2′-*O*-methyltransferase mutants replicated and spread in IFNAR-deficient mice. MHV-D130A was not detectable in spleens or livers of mice lacking either Mda5 or TLR7, which suggested that induction of the expression of type I interferon via either RNA sensor suffices to completely restrict the replication and spread of mutants with altered 2′-*O*-methyltransferase active sites. However, we were able to detect small amounts of the cap 0–binding mutant MHV-Y15A in the spleens of TLR7-deficient or Mda5-deficient mice, which suggested that lower induction of type I interferon in these mutant mice did not fully restrict replication of the virus with partially impaired 2′-*O*-methyltransferase. The replication and spread of the two MHV 2′-*O*-methyltransferase mutants in mice deficient in both TLR7 and Mda5 was indistinguishable from that in IFNAR-deficient mice. These observations confirm that TLR7 and Mda5 represent the main sensors for recognition of coronavirus RNA and demonstrate that 2′-*O*-methylation of viral mRNA serves as a mechanism by which viruses evade the recognition of non-self RNA by the host innate immune system *in vivo*.

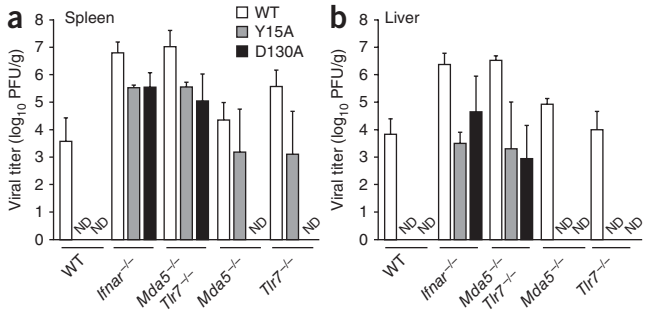

Figure 7 Deficiency in 2′-*O*-methyltransferase affects the recognition of virus by the innate immune system *in vivo*. Viral titers in the spleen (**a**) and liver (**b**) of wild-type mice and mice deficient in IFNAR, Mda5 or TLR7 or both Mda5 and TLR7, assessed 48 h after infection with MHV-A59, MHV-Y15A or MHV-D130A (500 plaque-forming units injected intraperitoneally). Data represent two independent experiments (mean and s.d. of six samples).

DISCUSSION

The correct functioning of host innate immune responses is based on reliable pathogen detection and is essential in limiting pathogen replication and spread. Using human and mouse coronavirus models of infection, we have shown here that 2′-*O*-methylation of mRNA provides a molecular signature with a dual role in the interaction with host innate immune responses. First, 2′-*O*-methylation of mRNA protects viral RNA from recognition by Mda5 and thus prevents Mda5-dependent production of type I interferon in virus-infected cells. Second, 2′-*O*-methylation of viral mRNA contributes to evasion of the interferon-mediated restriction of viral replication. These distinct effects can be uncoupled either in the absence of type I interferon signaling (such as in IFNAR-deficient cells or mice) or through a genetic approach that targets the cap 0–binding residue Tyr15 of MHV nsp16. The lack of 2′-*O*-methylation on a proportion of MHV-Y15A mRNA was sufficient to trigger the Mda5 pathway of the production of type I interferon while allowing the virus to evade the IFIT1-mediated restriction of viral replication. In contrast, the absence of 2′-*O*-methylation on the MHV-D130A viral RNA activated the Mda5 pathway and resulted in restriction of viral propagation.

Our study has described the effect of 2′-*O*-methylation of mRNA on Mda5-dependent induction of type I interferon. The use of coronavirus greatly facilitated this analysis because coronaviruses encode their own 5′ mRNA cap-methylation machinery, which allowed us to study the phenotype of recombinant viruses with mutant 2′-*O*-methyltransferase proteins, and because expression of type I interferon is almost undetectable in infected cells other than plasmacytoid dendritic cells, with the notable exception of macrophages, which produce small amounts of Mda5-mediated type I interferon after infection[23–25,29]. In contrast, most other RNA viruses that replicate in the cytoplasm induce considerable amounts of type I interferon, which may mask the specific effect of 2′-*O*-methylation of mRNA on Mda5 activation[2,30]. It will be important to clarify whether viral mRNA lacking 2′-*O*-methylation is directly recognized by Mda5, resulting in its activation, or whether 2′-*O*-methylation represents an activation signal for Mda5, possibly in combination with dsRNA regions. The generation of recombinant viruses with defined substitutions in RNA-processing enzymes, combined with biochemical approaches, will thus be useful in the identification of naturally occurring Mda5 ligands.

The evasion of Mda5-dependent RNA recognition and IFIT-dependent restriction of viral replication provide a reasonable explanation for the conservation of 2′-*O*-methyltransferases in many viruses that replicate in the cytoplasm of higher eukaryotes. Other viruses, such as bunyaviruses and arenaviruses, that replicate in the cytoplasm but have not acquired the ability to autonomously generate and modify their 5′ cap structures have evolved means for snatching the cap structure from cellular mRNA[31,32]. Moreover, structural and functional analyses have shown that the cap-binding nucleoprotein of Lassa virus (family Arenaviridae) can antagonize type I interferon through its associated 3′-to-5′ exoribonuclease activity, probably by cleaving RNAs that function as pathogen-associated molecular patterns[33]. This protein has an unusually deep cap-binding pocket proposed to accommodate an entire cap 1 structure[33] and could potentially discriminate between 2′-*O*-methylated and nonmethylated capped RNAs. Finally, members of the Picornavirales order and related viruses, which replicate in the cytoplasm but do not encode methyltransferases, have evolved alternative 5′ ends of their RNA. These viruses covalently attach a small viral protein (VPg) to the genomic 5′ terminus and have an internal ribosomal entry site at the 5′ untranslated region[34]. The replication of encephalomyocarditis virus (family Picornaviridae) seems to be not restricted by IFIT proteins[28]; however, infection with this virus is sensed through the Mda5 pathway[35]. Thus, we speculate that the use of internal ribosomal entry allows encephalomyocarditis virus to evade host restriction by IFIT family members, whereas the covalent attachment of VPg to the 5′ end of picornavirus RNA does not prevent Mda5-dependent recognition and induction of type I interferon.

The idea that RNA modification influence host cell innate immune responses is supported by the observation that activation of RIG-I and PKR is diminished when 5′-triphosphate RNA contains modified nucleotides[9,10,36]. Similarly, nucleoside modifications diminish the potential of RNA to trigger TLRs[37]. Although most of those observations were made *in vitro* (for example, by transfection of short synthetic RNA), it seems that RNA modifications may affect sensing by the innate immune system on a wider scale[38]. Therefore, it will be important to extend the knowledge of naturally occurring RNA modifications and their effect on innate immune responses. Other molecular RNA signatures that function as pathogen-associated molecular patterns will probably be discovered.

In summary, our study has identified 2′-*O*-methylation of eukaryotic mRNA cap structures as a molecular pattern of self mRNA and has demonstrated that there are at least two cellular mechanisms that allow the distinction of 2′-*O*-methylated mRNA versus nonmethylated mRNA. Consequently, many viruses that replicate in the cytoplasm, without access to the nuclear host cell machinery for mRNA capping and modification, have evolved their own RNA-modifying enzymes as means of mimicking cellular mRNA. Our data should encourage further studies to evaluate the full spectrum and functional importance of mRNA modifications as an additional layer of information ‘imprinted’ on eukaryotic mRNA.

METHODS

Methods and any associated references are available in the online version of the paper at http://www.nature.com/natureimmunology/.

Note: Supplementary information is available on the Nature Immunology website.

ACKNOWLEDGMENTS

We thank V. Lohmann (University of Heidelberg) for Huh-7 cells; G.L. Smith (Imperial College, London) for D980R cells; S.G. Sawicki (Medical University of Ohio) for 17Cl1 cells; M. Pelegrin (Institut de Génétique Moléculaire de Montpellier) for LL171 cells; L. Onder for assistance with fluorescence microscopy; and R. de Giuli, B. Schelle and N. Karl for technical assistance. This study was supported by the Swiss National Science Foundation, the European Commission (TOLERAGE), the Novartis Foundation for Biomedical Research, Switzerland, the German Ministry of Education and Research (V.T.), the Austrian Science Fund (FWF J3044 to M.H.), Deutsche Forschungsgemeinschaft (J.Z.), the National Institutes of Health (AI060915 and AI085089 to S.C.B.; U54 AI081680 (Pacific Northwest Regional Center of Excellence for Biodefense and Emerging Infectious Diseases Research to M.S.D), the Medical Research Council (B.W.N.) and the Wellcome Trust (S.G.S.).

AUTHOR CONTRIBUTIONS

R.Z., L.C.-B., M.H., R.M. and K.J.S. did most of the experiments; B.W.N. did phylogenetic analyses; B.W.N. and S.C.B. did electron microscopy; J.Z., S.C.B., W.B., M.S.D., S.G.S. and B.L. contributed reagents and expertise; and S.G.S., B.W.N., B.L. and V.T. conceived of and designed the project and wrote and edited the manuscript.

COMPETING FINANCIAL INTERESTS

The authors declare no competing financial interests.

Published online at http://www.nature.com/natureimmunology/.
Reprints and permissions information is available online at http://npg.nature.com/reprintsandpermissions/.

1. Janeway, C.A. Jr. Approaching the asymptote? Evolution and revolution in immunology. *Cold Spring Harb. Symp. Quant. Biol.* **54**, 1–13 (1989).
2. Takeuchi, O. & Akira, S. Innate immunity to virus infection. *Immunol. Rev.* **227**, 75–86 (2009).

3. Loo, Y.M. & Gale, M. Jr. Viral regulation and evasion of the host response. *Curr. Top. Microbiol. Immunol.* **316**, 295–313 (2007).
4. Haller, O. & Weber, F. Pathogenic viruses: smart manipulators of the interferon system. *Curr. Top. Microbiol. Immunol.* **316**, 315–334 (2007).
5. Hui, D.J., Terenzi, F., Merrick, W.C. & Sen, G.C. Mouse p56 blocks a distinct function of eukaryotic initiation factor 3 in translation initiation. *J. Biol. Chem.* **280**, 3433–3440 (2005).
6. Terenzi, F., Hui, D.J., Merrick, W.C. & Sen, G.C. Distinct induction patterns and functions of two closely related interferon-inducible human genes, ISG54 and ISG56. *J. Biol. Chem.* **281**, 34064–34071 (2006).
7. Fensterl, V. & Sen, G.C. The ISG56/IFIT1 gene family. *J. Interferon Cytokine Res.* published online, doi:10.1089/jir.2010.0101 (25 October 2010).
8. Kato, H. *et al.* Length-dependent recognition of double-stranded ribonucleic acids by retinoic acid-inducible gene-I and melanoma differentiation-associated gene 5. *J. Exp. Med.* **205**, 1601–1610 (2008).
9. Hornung, V. *et al.* 5′-triphosphate RNA is the ligand for RIG-I. *Science* **314**, 994–997 (2006).
10. Pichlmair, A. *et al.* RIG-I-mediated antiviral responses to single-stranded RNA bearing 5′-phosphates. *Science* **314**, 997–1001 (2006).
11. Schlee, M. *et al.* Recognition of 5′ triphosphate by RIG-I helicase requires short blunt double-stranded RNA as contained in panhandle of negative-strand virus. *Immunity* **31**, 25–34 (2009).
12. Ghosh, A. & Lima, C.D. Enzymology of RNA cap synthesis. *WIREs RNA* **1**, 152–172 (2010).
13. Shuman, S. What messenger RNA capping tells us about eukaryotic evolution. *Nat. Rev. Mol. Cell Biol.* **3**, 619–625 (2002).
14. Nomoto, A., Detjen, B., Pozzatti, R. & Wimmer, E. The location of the polio genome protein in viral RNAs and its implication for RNA synthesis. *Nature* **268**, 208–213 (1977).
15. Hemmi, H. *et al.* A Toll-like receptor recognizes bacterial DNA. *Nature* **408**, 740–745 (2000).
16. Bouvet, M. *et al.* In vitro reconstitution of SARS-coronavirus mRNA cap methylation. *PLoS Pathog.* **6**, e1000863 (2010).
17. Chen, Y. *et al.* Functional screen reveals SARS coronavirus nonstructural protein nsp14 as a novel cap N7 methyltransferase. *Proc. Natl. Acad. Sci. USA* **106**, 3484–3489 (2009).
18. Decroly, E. *et al.* Coronavirus nonstructural protein 16 is a cap-0 binding enzyme possessing (nucleoside-2′-*O*)-methyltransferase activity. *J. Virol.* **82**, 8071–8084 (2008).
19. Snijder, E.J. *et al.* Unique and conserved features of genome and proteome of SARS-coronavirus, an early split-off from the coronavirus group 2 lineage. *J. Mol. Biol.* **331**, 991–1004 (2003).
20. Feder, M., Pas, J., Wyrwicz, L.S. & Bujnicki, J.M. Molecular phylogenetics of the RrmJ/fibrillarin superfamily of ribose 2′-*O*-methyltransferases. *Gene* **302**, 129–138 (2003).
21. Schnierle, B.S., Gershon, P.D. & Moss, B. Cap-specific mRNA (nucleoside-*O*2′-)-methyltransferase and poly(A) polymerase stimulatory activities of vaccinia virus are mediated by a single protein. *Proc. Natl. Acad. Sci. USA* **89**, 2897–2901 (1992).
22. Cervantes-Barragán, L. *et al.* Type I IFN-mediated protection of macrophages and dendritic cells secures control of murine coronavirus infection. *J. Immunol.* **182**, 1099–1106 (2009).
23. Cervantes-Barragan, L. *et al.* Control of coronavirus infection through plasmacytoid dendritic-cell-derived type I interferon. *Blood* **109**, 1131–1137 (2007).
24. Rose, K.M., Elliott, R., Martinez-Sobrido, L., Garcia-Sastre, A. & Weiss, S.R. Murine coronavirus delays expression of a subset of interferon-stimulated genes. *J. Virol.* **84**, 5656–5669 (2010).
25. Roth-Cross, J.K., Bender, S.J. & Weiss, S.R. Murine coronavirus mouse hepatitis virus is recognized by MDA5 and induces type I interferon in brain macrophages/microglia. *J. Virol.* **82**, 9829–9838 (2008).
26. Zhou, H., Zhao, J. & Perlman, S. Autocrine interferon priming in macrophages but not dendritic cells results in enhanced cytokine and chemokine production after coronavirus infection. *MBio* **1**, e00219–10 (2010).
27. Bocharov, G. *et al.* A systems immunology approach to plasmacytoid dendritic cell function in cytopathic virus infections. *PLoS Pathog.* **6**, e1001017 (2010).
28. Daffis, S. *et al.* 2′-O methylation of the viral mRNA cap evades host restriction by IFIT family members. *Nature* **468**, 452–456 (2010).
29. Thiel, V. & Weber, F. Interferon and cytokine responses to SARS-coronavirus infection. *Cytokine Growth Factor Rev.* **19**, 121–132 (2008).
30. Loo, Y.M. *et al.* Distinct RIG-I and MDA5 signaling by RNA viruses in innate immunity. *J. Virol.* **82**, 335–345 (2008).
31. Morin, B. *et al.* The N-terminal domain of the arenavirus L protein is an RNA endonuclease essential in mRNA transcription. *PLoS Pathog.* **6**, e1001038 (2010).
32. Reguera, J., Weber, F. & Cusack, S. Bunyaviridae RNA polymerases (L-protein) have an N-terminal, influenza-like endonuclease domain, essential for viral cap-dependent transcription. *PLoS Pathog.* **6**, e1001101 (2010).
33. Qi, X. *et al.* Cap binding and immune evasion revealed by Lassa nucleoprotein structure. *Nature* advance online publication, doi:10.1038/nature09605 (17 November 2010).
34. Le Gall, O. *et al.* Picornavirales, a proposed order of positive-sense single-stranded RNA viruses with a pseudo-T = 3 virion architecture. *Arch. Virol.* **153**, 715–727 (2008).
35. Gitlin, L. *et al.* Essential role of mda-5 in type I IFN responses to polyriboinosinic: polyribocytidylic acid and encephalomyocarditis picornavirus. *Proc. Natl. Acad. Sci. USA* **103**, 8459–8464 (2006).
36. Nallagatla, S.R. & Bevilacqua, P.C. Nucleoside modifications modulate activation of the protein kinase PKR in an RNA structure-specific manner. *RNA* **14**, 1201–1213 (2008).
37. Karikó, K., Buckstein, M., Ni, H. & Weissman, D. Suppression of RNA recognition by Toll-like receptors: the impact of nucleoside modification and the evolutionary origin of RNA. *Immunity* **23**, 165–175 (2005).
38. Nallagatla, S.R., Toroney, R. & Bevilacqua, P.C. A brilliant disguise for self RNA: 5′-end and internal modifications of primary transcripts suppress elements of innate immunity. *RNA Biol.* **5**, 140–144 (2008).

ONLINE METHODS

Mice, viruses, cells and viral infection. C57BL/6 mice were from Charles River Laboratories. Immunodeficient mice deficient in IFNAR, Mda5 or TLR7 or both Mda5 and TLR7 on the C57BL/6 background were bred in the animal facilities of the Kantonal Hospital St. Gallen. IFIT1-deficient mice were bred in the animal facilities of the Washington University School of Medicine. All mice were maintained in individually ventilated cages and were used between 6 and 9 weeks of age. All animal experiments were done in accordance with the Swiss Federal legislation and with approval from the animal studies committees of the Cantonal Veterinary Office (St. Gallen, Switzerland) and St. Louis University.

The HCoV-229E, HCoV-D129A, MHV strain A59, MHV-D130A and MHV-Y15A recombinant viruses were generated with a vaccinia virus–based reverse-genetic system as described[39] and were propagated on Huh-7 hepatocarcinoma cells (HCoV) or 17Cl1 mouse fibroblasts (MHV). BHK-21 baby hamster kidney cells, L929 mouse fibroblasts, NIH3T3 mouse fibroblasts, MRC-5 human fetal lung cells and CV-1 monkey kidney fibroblasts were from the European Collection of Cell Cultures. Huh-7 cells were a gift from V. Lohmann; D980R human epithelial cells were a gift from G.L. Smith; and 17Cl1 cells were a gift from S.G. Sawicki. All cells were maintained in minimal essential medium supplemented with 5–10% (vol/vol) FBS and antibiotics. Thioglycollate-elicited mouse macrophages were generated as described[40]. Human macrophages were isolated from peripheral blood of normal donors as described[41]. Experiments using human cells were in compliance with the Swiss federal legislation and institutional guidelines of the Kantonsspital St.Gallen (including informed consent) and were appoved by the ethical committee of Canton St. Gallen, Switzerland.

Mice were injected intraperitoneally with 500 plaque-forming units of MHV. Organs were stored at −70 °C until further analysis. Human blood-derived macrophages and thioglycolate-elicited mouse macrophages (0.5×10^6 to 1×10^6) were infected at the appropriate MOI in a 24-well format. MHV titers were determined by standard plaque assay with L929 cells. HCoV titers were determined by plaque assay with Huh-7 cells overlaid at 1 h after infection with 1.2% (wt/vol) Avicel microcrystalline cellulose in 10% (vol/vol) DMEM and stained with crystal violet 3 d after infection.

***In vitro* 2′-O-methylation of poly(A)-containing RNA.** Poly(A)-containing RNA was isolated from 1×10^7 mock- or HCoV-infected Huh-7 cells (MOI = 1; isolated 48 h after infection) or 1×10^7 mock- or MHV-infected NIH-3T3 cells (MOI = 1; isolated 24 h after infection) with the Dynabeads mRNA DIRECT kit according to the manufacturer's recommendations (Invitrogen). RNA was precipitated after the addition of 0.1 volume of 4 M ammonium acetate and 1 volume of isopropanol, then was washed with 70% ethanol and dissolved in 10 mM TRIS-HCl, pH 7.5, to a final concentration of 150 ng/μl. *In vitro* 2′-*O*-methylation reactions were incubated for 1 h at 37 °C and included 300 ng poly(A)-containing RNA derived from virus-infected cells or the corresponding amount of poly(A)-containing RNA from uninfected cells (as determined by quantitative RT-PCR with primers specific for mouse GAPDH and human β-actin; data not shown) plus ScriptCap 2′-*O*-methyltransferase (Epicentre Biotechnologies) in 0.5 μM *S*-adenosyl-methionine and 1.4 μM ^{3}H-labeled *S*-adenosyl-methionine (78 Ci/mmol; Perkin Elmer). Reactions were purified with SigmaSpin Post-Reaction Clean-Up columns (Sigma-Aldrich) and eluates were mixed with 2 ml Ultima Gold scintillation fluid for measurement of ^{3}H incorporation with a Packard Tri-Carb liquid scintillation counter (Perkin Elmer).

Immunofluorescence, IFN-β enzyme-linked immunosorbent assay and IFN-α pretreatment. IRF3 was detected in mouse macrophages (2×10^5 cells per well in 200 μl) 3 h after infection with MHV at an MOI of 1. Cells were stained with antibody to IRF3 (FL-425; Santa Cruz Biotechnology) and with DAPI (4,6-diamidino-2-phenylindole). Images were acquired with a DMRA microscope (Leica). The concentration of mouse and human IFN-β in cell culture supernatants was measured by enzyme-linked immunosorbent assay (PBL Biomedical Laboratories). Universal type I interferon (IFN-α A/D; Sigma) was used for pretreatment of cells with IFN-α before viral infection.

Bioassay for type I interferon. Total type I interferon in supernatants was measured with LL171 cells (a gift from M. Pelegrin), which are L929 cells stably transfected with a luciferase reporter plasmid under control of the interferon-stimulated response element[42]. Recombinant IFN-α A/D (Sigma) was used as a cytokine standard. Before measurement, virus was removed by centrifugation of supernatants through AMICON spin columns with a cutoff of 100 kilodaltons (Millipore). LL171 cells grown in 96-well plates were treated for 6 h with column-filtered supernatants, and luciferase activity was detected by a GloMax 96 Microplate Luminometer (Promega) after the addition of Bright-Glo Luciferase substrate (Promega).

Quantitative RT-PCR. Total cellular RNA was isolated with a NucleoSpin RNA II kit according to the manufacturer's instructions (Macherey-Nagel) and was used as template for cDNA synthesis with a High Capacity cDNA Reverse Transcription kit (Applied Biosystems). A LightCycler FastStart DNA Master SYBR Green I kit (Roche) and a LightCycler 1.5 (Roche) were used for measurement of mRNA for IFN-β and TATA box–binding protein with the following primers: IFN-β, 5′-GGTGGAATGAGACTATTGTTG-3′ and 5′-AGGACATCTCCCACGTC-3′; TATA box–binding protein, 5′-CCTTCACCAATGACTCCTATGAC-3′ and 5′-CAAGTTTACAGCCAAGATTCAC-3′. Measurements were made in duplicate and the expression of IFN-β was normalized to that in uninfected cells by the comparative cycling threshold method ($\Delta\Delta C_T$).

Phylogenetic analysis of viral methyltransferase domains. Regions of methyltransferase homology have been identified as members of the RrmJ-like superfamily (InterPro accession code IPR002877). For viruses with no RrmJ-like domain, secondary structure–assisted alignment of amino acids was done to determine whether a distant homolog might be present. Viruses without identification of a primary or secondary structure match to RrmJ-like proteins are designated 'not detected' (**Supplementary Table 1**). Amino acid sequences were aligned with ClustalW2 and were manually adjusted on the basis of published structural data and protein secondary structure predictions of the PSIPRED server[43]. Motif nomenclature was as published[44]. Amino acids were assigned colors according the conventions of ClustalX for amino acid similarity and conservation as implemented in the JalView alignment editor[45].

Electron microscopy. Ultrathin sections of mouse L929 cells were stained with osmium tetroxide and uranyl acetate 5 h after infection with MHV at an MOI of 1 and images were obtained by transmission electron microscopy as described[46].

39. Eriksson, K.K., Makia, D. & Thiel, V. Generation of recombinant coronaviruses using vaccinia virus as the cloning vector and stable cell lines containing coronaviral replicon RNAs. *Methods Mol. Biol.* **454**, 237–254 (2008).
40. Züst, R. *et al.* Coronavirus non-structural protein 1 is a major pathogenicity factor: implications for the rational design of coronavirus vaccines. *PLoS Pathog.* **3**, e109 (2007).
41. Wünschmann, S., Becker, B. & Vallbracht, A. Hepatitis A virus suppresses monocyte-to-macrophage maturation in vitro. *J. Virol.* **76**, 4350–4356 (2002).
42. Uzé, G. *et al.* Domains of interaction between α interferon and its receptor components. *J. Mol. Biol.* **243**, 245–257 (1994).
43. Bryson, K. *et al.* Protein structure prediction servers at University College London. *Nucleic Acids Res.* **33**, W36–W38 (2005).
44. Fauman, E.B., Blumenthal, R.M. & Cheng, X. Structure and Evolution of AdoMet-Dependent Methyltransferases. in *S-Adenosylmethionine-Dependent Methyltransferases: Structures and Functions* (eds. Cheng, X. & Blumenthal, R.M.) 1–38 (World Scientific, Singapore, 1999).
45. Waterhouse, A.M., Procter, J.B., Martin, D.M., Clamp, M. & Barton, G.J. Jalview Version 2—a multiple sequence alignment editor and analysis workbench. *Bioinformatics* **25**, 1189–1191 (2009).
46. Gosert, R., Kanjanahaluethai, A., Egger, D., Bienz, K. & Baker, S.C. RNA replication of mouse hepatitis virus takes place at double-membrane vesicles. *J. Virol.* **76**, 3697–3708 (2002).

doi:10.1038/ni.1979